





# Interferon- $\gamma$ drives macrophage reprogramming, cerebrovascular remodelling, and cognitive dysfunction in a zebrafish and a mouse model of ion imbalance and pressure overload

Dilem C. Apaydin<sup>1,2</sup>, Bhakti I. Zakarauskas-Seth<sup>1,3†</sup>, Lorenzo Carnevale <sup>4†</sup>,  
Onur Apaydin<sup>1,2</sup>, Marialuisa Perrotta<sup>4,5</sup>, Raimondo Carnevale <sup>4</sup>, Maria P. Kotini<sup>6</sup>,  
Ilan Kotlar-Goldaper<sup>1,3</sup>, Heinz-Georg Belting<sup>6</sup>, Daniela Carnevale <sup>4,5†</sup>,  
Alessandro Filosa<sup>1†</sup>, and Suphansa Sawamiphak <sup>1,7\*</sup>

<sup>1</sup>Max Delbrück Center (MDC), Robert-Rössle-Str. 10, 13125 Berlin, Germany; <sup>2</sup>Institute of Chemistry and Biochemistry, Department of Biology, Chemistry and Pharmacy, Freie Universität Berlin, Berlin, Germany; <sup>3</sup>Charité—Universitätsmedizin Berlin, Corporate member of Freie Universität Berlin and Humboldt Universität zu Berlin, Berlin, Germany; <sup>4</sup>Unit of Neuro and Cardiovascular Pathophysiology, IRCCS Neuromed, Pozzilli (Isernia), Italy; <sup>5</sup>Department of Molecular Medicine, Sapienza University of Rome, Rome, Italy; <sup>6</sup>Department of Cell Biology, Biozentrum, University of Basel, Basel, Switzerland; and <sup>7</sup>DZHK (German Center for Cardiovascular Research), Partner Site Berlin, Geschäftsstelle Potsdamer Str. 58, 10785 Berlin, Germany

Received 25 January 2022; revised 24 September 2022; accepted 21 October 2022; online publish-ahead-of-print 20 December 2022

**Aims** Dysregulated immune response contributes to inefficiency of treatment strategies to control hypertension and reduce the risk of end-organ damage. Uncovering the immune pathways driving the transition from the onset of hypertensive stimulus to the manifestation of multi-organ dysfunction are much-needed insights for immune targeted therapy.

**Methods and results** To aid visualization of cellular events orchestrating multi-organ pathogenesis, we modelled hypertensive cardiovascular remodelling in zebrafish. Zebrafish larvae exposed to ion-poor environment exhibited rapid angiotensinogen up-regulation, followed by manifestation of arterial hypertension and cardiac remodelling that recapitulates key characteristics of incipient heart failure with preserved ejection fraction. In the brain, time-lapse imaging revealed the occurrence of cerebrovascular regression through endothelial retraction and migration in response to the ion-poor treatment. This phenomenon is associated with macrophage/microglia-endothelial contacts and endothelial junctional retraction. Cytokine and transcriptomic profiling identified systemic up-regulation of interferon- $\gamma$  and interleukin 1 $\beta$  and revealed altered macrophage/microglia transcriptional programme characterized by suppression of innate immunity and vasculo/neuroprotective gene expression. Both zebrafish and a murine model of pressure overload-induced brain damage demonstrated that the brain pathology and macrophage/microglia phenotypic alteration are dependent on interferon- $\gamma$  signalling. In zebrafish, interferon- $\gamma$  receptor 1 mutation prevents cerebrovascular remodelling and dysregulation of macrophage/microglia transcriptomic profile. Supplementation of bone morphogenetic protein 5 identified from the transcriptomic approach as a down-regulated gene in ion-poor-treated macrophages/microglia that is rescued by interferon- $\gamma$  blockage, mitigated cerebral microvessel loss. In mice subjected to transverse aortic constriction-induced pressure overload, typically developing cerebrovascular injury, neuroinflammation, and cognitive dysfunction, interferon- $\gamma$  neutralization protected them from blood–brain barrier disruption, cerebrovascular rarefaction, and cognitive decline.

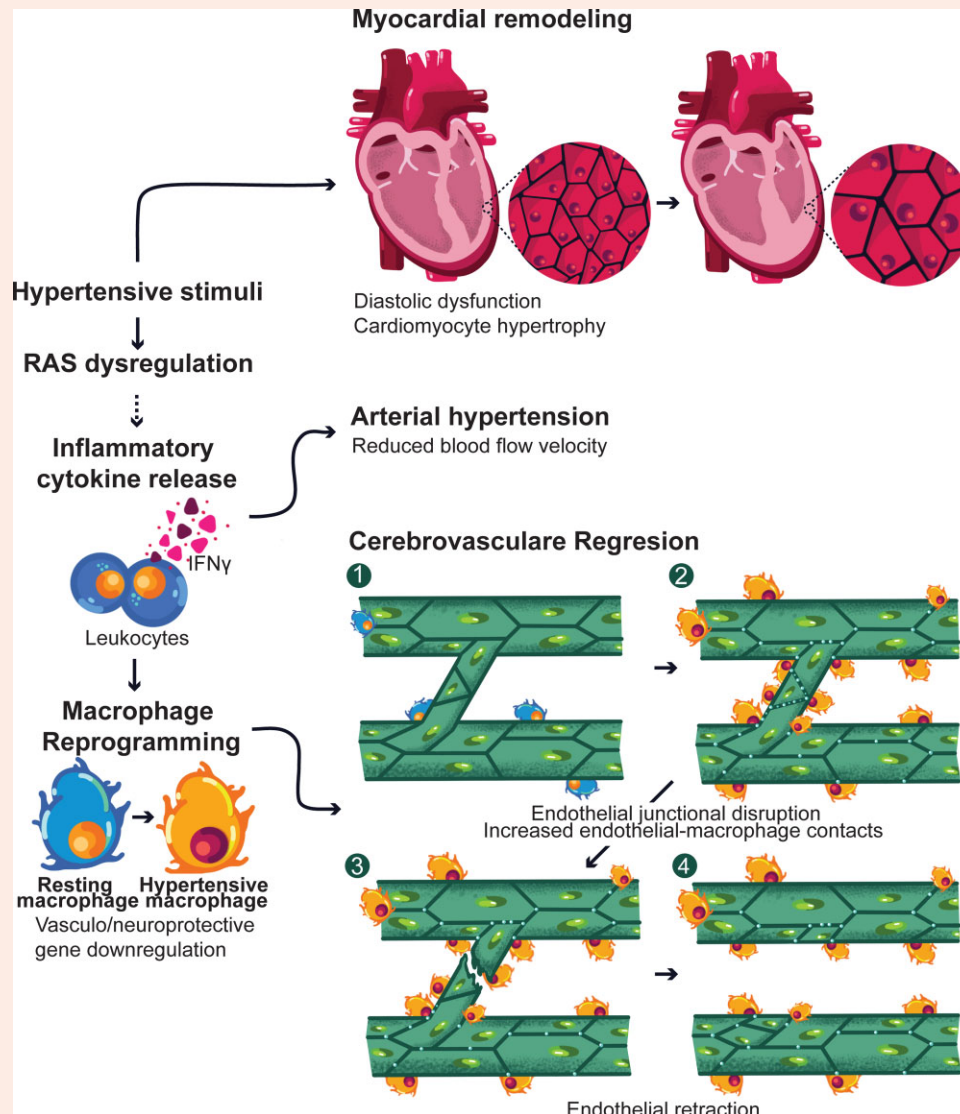
**Conclusions** These findings uncover cellular and molecular players of an immune pathway communicating hypertensive stimulus to structural and functional remodelling of the brain and identify anti-interferon- $\gamma$  treatment as a promising intervention strategy capable of preventing pressure overload-induced damage of the cerebrovascular and nervous systems.

\* Corresponding author. Tel: +49 30 9406-3680, E-mail: [Suphansa.Sawamiphak@mdc-berlin.de](mailto:Suphansa.Sawamiphak@mdc-berlin.de)

† These authors contributes equally to the work.

© The Author(s) 2022. Published by Oxford University Press on behalf of the European Society of Cardiology. All rights reserved. For permissions, please email: [journals.permissions@oup.com](mailto:journals.permissions@oup.com).

## Graphical Abstract



## Keywords

zebrafish • hypertension • diastolic dysfunction • vascular regression • inflammation • macrophage • IFN $\gamma$  • cerebrovascular disease • cognitive impairment

## 1. Introduction

Hypertension is the most prevalent chronic disease and a major health challenge.<sup>1,2</sup> Although elevated blood pressure is the key diagnostic feature of hypertension, its mortality and disability are results of associated cardiovascular comorbidities such as heart failure, stroke, chronic kidney disease, and cognitive impairment.<sup>3</sup> Current treatment strategies mainly target the key regulatory pathways controlling physiological blood pressure, the sympathetic nervous system, and the renin (Ren) angiotensin (Agt) system.<sup>3,4</sup> While these drugs help in reaching target blood pressure levels in a consistent proportion of patients with essential hypertension, it is still difficult to hamper the progression of target organ damage. This is particularly true for cerebrovascular alterations. It is also becoming increasingly clear that, even in subjects with acceptable blood pressure levels, an elevated residual risk of cardiovascular events may persist,<sup>5,6</sup> highlighting the existence of additional disease drivers.

A pivotal contribution of systemic inflammation and immune reactivity in the pathogenesis of hypertension and end-organ damage is well-recognized.<sup>7,8</sup> Diverse types of innate and adaptive immune cells, and cytokines they secrete, have been shown to participate in pathogenesis of hypertension.<sup>7-11</sup> However, our mechanistic understanding of how activation of these immune cells can lead to the onset and progression of hypertension is still lacking. It is commonly viewed that innate immune cells, as initiators of inflammatory response to hypertensive stimuli, play a key role in vascular injury. Monocyte/macrophage deficiency mitigates the effect of angiotensin II (Ang II),<sup>10,12</sup> aldosterone,<sup>13</sup> and endothelin-1<sup>14</sup> to induce vascular dysfunction and oxidative stress in resistance arteries and aortas. Similarly, ablation of perivascular macrophages in the brain prevents structural and functional remodelling of the middle cerebral artery and cerebrovascular oxidative stress in murine models of hypertension.<sup>15,16</sup> Deleterious effects of immune cells in hypertension do not depend solely

on production of pro-inflammatory cytokines or reactive oxygen species. It has been shown that interleukin (IL) 10 production by a macrophage subset accumulating in the heart upon aldosterone and salt-induced hypertension promoted cardiac fibrosis and diastolic dysfunction.<sup>17</sup>

Collectively, a body of evidence demonstrating interactions of different immune cell types with the vasculature, the heart, and the brain suggests an overarching hypothesis that dysregulated immune cells drive hypertension development by disrupting blood pressure-regulatory functions of these organs.<sup>3,4,18</sup> However, end organ malfunction can provoke inflammation in various peripheral tissues, implicating complex cascades of immune reactivity both as causes and consequences of hypertension.<sup>19,20</sup> A better understanding of the site-specific effects of diverse immune cell subsets as well as mechanistic insight into the immune pathways communicating hypertensive signals to the affected organs is fundamental for the development of immune-targeting strategies to manage clinical hypertension.

Here, we tackled three main questions: (i) cellular processes underlying immune cell-driven adverse remodelling of the blood-pressure-regulating organs; (ii) molecular mediator of the cellular events; and (iii) if manipulation of the identified immune pathway can prevent development of hypertension and end-organ pathological remodelling. By introducing ion-poor-induced disturbance of body fluid homeostasis, we established zebrafish as a new model that recapitulates the multi-systemic structural and functional remodelling characteristics of human hypertension, with the advantage of requiring simpler manipulations and shorter treatment time than currently available rodent models.<sup>2</sup> Importantly, the model allows not only post-mortem characterization of the multi-systemic phenotypes of hypertension but also a live imaging approach to trace cellular behaviours during pathogenic progression. Exploiting the zebrafish model, we were able to uncover the cellular processes occurring during the transition from exposure to ion imbalance stimulus to manifestation of brain pathology, i.e. macrophage/microglia-endothelial cell contacts and endothelial junctional disruption that precede endothelial cell migration-driven cerebrovascular regression and increased cell death in the brain. Mechanistically, we identify interferon- $\gamma$  (IFN $\gamma$ ) signalling acting as a crucial mediator of systemic inflammation-driven arterial dysfunction and ion imbalance-driven brain remodelling. In response to the ion-poor exposure, IFN $\gamma$  signals down-regulation of homeostatic, pro-angiogenic, and neuro-protective factors in macrophage/microglia. We showed that one of the factors, bone morphogenic protein (BMP) 5, participates in the IFN $\gamma$ -driven pathogenic pathway. Finally, in a murine model of cardiac pressure overload-induced brain pathology, we provide a proof of concept of inflammation-targeted therapy that can abrogate cerebrovascular rarefaction, blood-brain barrier (BBB) and endothelial junctional disruption, and cognitive dysfunction.

## 2. Methods

Detailed material and methods are available in the [Supplementary material online, Data Supplement](#). Zebrafish husbandry and experiments were performed under standard conditions in accordance with institutional (Max Delbrück Center for Molecular Medicine), State (LAGeSo Berlin), and German ethical and animal welfare guidelines, and approved by LAGeSo Berlin. All experiments were performed on larvae up to 10 days post fertilization (dpf). Fish larvae were euthanized by anaesthesia with 0.168 mg/ml tricaine methanesulfonate (MS-222), followed by immersion in ice water to induce hypothermia. Zebrafish experiments at the Biozentrum of the University of Basel were performed in accordance with federal guidance and approved by the Kantonales Veterinäramt of Kanton Basel-Stadt (1041G and 1041H). Zebrafish were maintained in standard conditions.<sup>21</sup>

All murine experiments were performed according to the EC Council Directive 2010/63 and Italian D.Lgs 26/2014, approved by the Institutional Animal Care and Use Committee at I.R.C.C.S. Neuromed, and authorized by the Italian Ministry of Health (Auth. Number 842/2020-PR), with procedures designed to minimize animal suffering and respecting the 3Rs principles. Mice were anaesthetized with a mixture of

ketamine/xylazine and transcardially perfused with 40 mL of saline solution followed by 40 mL of 4% paraformaldehyde and then euthanized by cervical dislocation.

## 3. Results

### 3.1 Establishment of an ion homeostatic imbalance paradigm to model arterial hypertension in zebrafish larvae

To facilitate examination of cellular and molecular mechanisms orchestrating the onset of hypertension and associated cardiovascular complications, we have established a zebrafish model capable of capturing hallmarks of hypertension and associated organ damage with minimal manipulations. We adapted an ion-poor treatment approach previously demonstrated to acutely induce renin angiotensin system (RAS)-dependent Na<sup>+</sup> uptake.<sup>22</sup> Our approach has three main advantages over other hypertensive models. First, it relies on systemic adaptation to environmental cues, not requiring genetic or surgical manipulations, as found in human hypertension. Second, the treatment time is very short. Third, the use of zebrafish at larval stages allows the use of live imaging methods to discover cellular mechanisms underlying the pathology. Starting at 2 dpf, embryos were reared in Danieau's buffer diluted in deionized water to a concentration of 1:750 until 4 dpf (Figure 1A). After 2 days, the concentration was reduced to 1:1500 and larvae were further treated until 7 dpf (Figure 1A).

To test whether the ion-poor treatment leads to increased arterial pressure, we measured flow velocity in the dorsal aorta. Decreased flow velocity in different arterial vascular beds is strongly associated with blood pressure rise in patient studies.<sup>23–26</sup> Accordingly, we observed significant reduction of end diastolic (Figure 1B and C) and, to a lesser extent, peak systolic velocity (Figure 1B and D) measured in the dorsal aorta, suggesting an increase of arterial pressure and/or resistance. Arterial resistive index, an indicative parameter of altered vascular resistance and compliance associated with arterial stiffness in hypertensive patients,<sup>23</sup> was also elevated in ion-poor treated larvae (Figure 1E).

### 3.2 RAS dysregulation mediates ion imbalance-induced arterial dysfunction

RAS, a key control system for blood pressure regulation and electrolyte homeostasis, is fundamental to pathogenesis of hypertension.<sup>27</sup> Thus, we next examined whether RAS dysregulation takes part in the ion-poor induced vascular response by delineating the time line and relationship of Agt and Ren induction prior to the onset of overt symptoms. To this end, we assessed by quantitative reverse transcriptase-polymerase chain reaction (qRT-PCR) time course expression of both genes in larvae exposed to ion-poor treatment during initiation of the pathogenic cascade (2–5 dpf). Significant elevation of *agt* messenger RNA level was detectable after 2 days of ion-poor treatment, while level of *ren* expression was unchanged at this stage (Figure 1F). *agt* expression increased further at 3 days of treatment when *ren* elevation was also detectable (Figure 1F). Furthermore, we investigated the effect of RAS antagonism on the change of arterial flow. Treatment with losartan, a competitive Ang II receptor type 1 antagonist, during early stage of ion-poor exposure at 2–5 dpf (Figure 1G) indeed attenuated the effect of the stimulus on the reduction of arterial flow velocity measured in diastole, and elevation of arterial resistive index (Figure 1H–K). We also examined the effect of late losartan administration at 4–7 dpf during ion-poor exposure (Figure 1G). Interestingly, this late intervention was unable to alleviate the arterial pressure/resistance phenotype induced by ion-poor treatment (Figure 1H–K).

Together, the data highlight the usefulness of the new experimental model to capture both phenotypic and molecular characteristics of human hypertension. Furthermore, these findings indicate that ion-poor induction of ion homeostatic disruption leads to phenotypic manifestation of arterial hypertension initially through RAS dysregulation. Blockage of RAS activation can prevent the progression from the early onset of the pathogenic

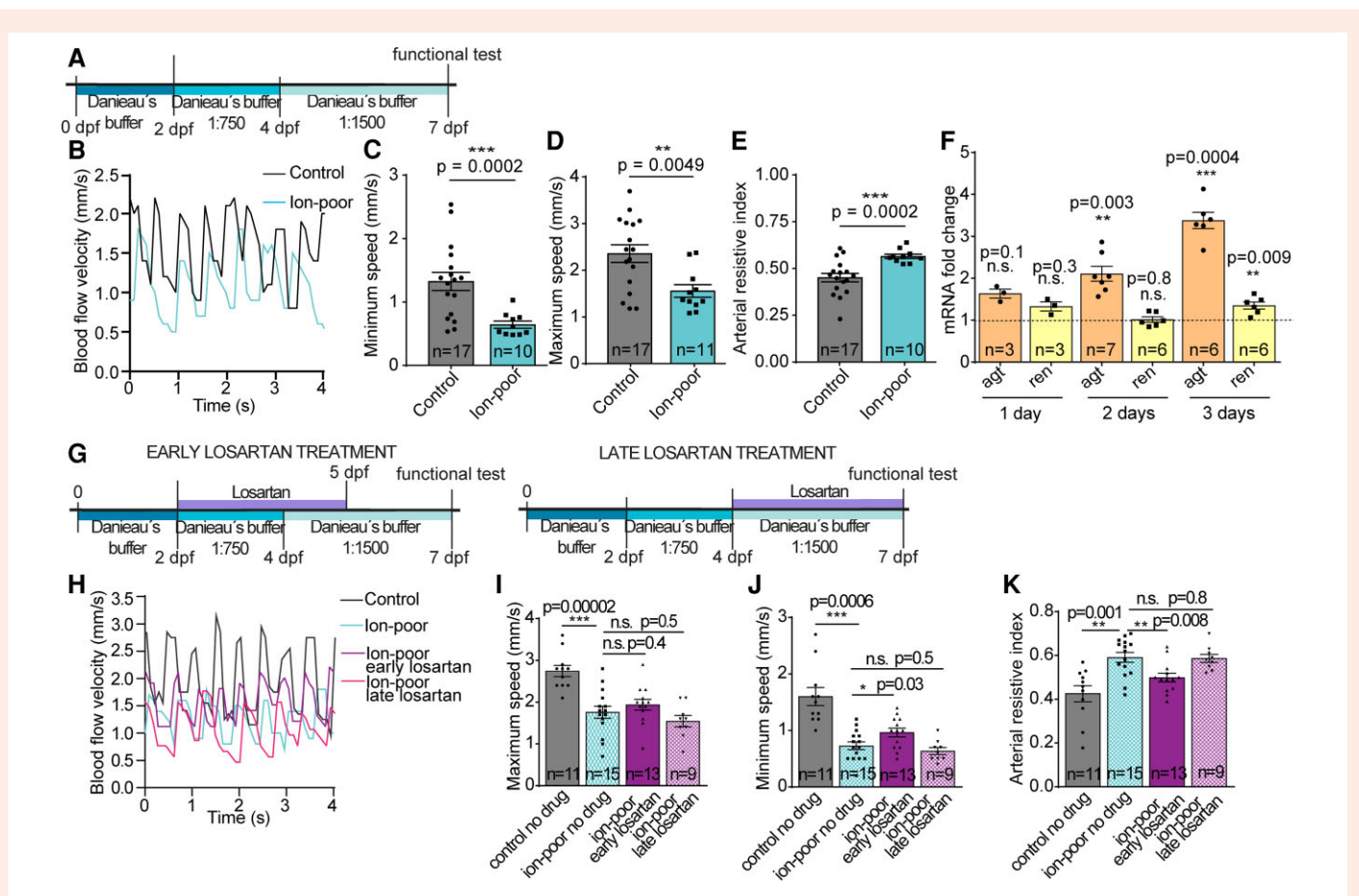


**Figure 1** Exposure to ion-poor treatment induces hallmarks of arterial hypertension in zebrafish larvae through RAS dysregulation. **A**, Schematic illustration of the 5-day hypotonic treatment paradigm for zebrafish larvae. **B**, Line graph depicting blood flow velocities of a representative control and an ion-poor-treated larva over time. **C–E**, Bar graphs showing lower end diastolic velocity (**C**), peak systolic velocity (**D**), and higher arterial resistive index (**E**) in ion-poor-treated larvae, compared to control siblings.  $n_{\text{control}} = 17$  larvae,  $n_{\text{ion-poor}} = 10$  (**E**) or 11 (**D**) larvae. **F**, *agt* and *ren* mRNA levels assessed by qRT-PCR at 1, 2, and 3 days of ion-poor treatment showed progressive induction of *agt* expression. *ren* induction was also detectable at day 3.  $n_{\text{agt},1 \text{ day}} = 3$  biological replicas (pooled larvae),  $n_{\text{ren},1 \text{ day}} = 3$  biological replicas,  $n_{\text{agt},2 \text{ days}} = 7$  biological replicas,  $n_{\text{ren},2 \text{ days}} = 6$  biological replicas,  $n_{\text{agt},3 \text{ days}} = 6$  biological replicas,  $n_{\text{ren},3 \text{ days}} = 6$  biological replicas. **G**, Schematic illustration of early and late treatment of the RAS antagonist losartan. **H**, Line graph presenting alleviation of ion-poor induction of decreased blood flow velocities by early treatment of losartan in representative control, ion-poor treated, ion-poor and early losartan treated, and ion-poor and late losartan treated larvae. **I–K**, Bar graphs showing effectiveness of early, but not late losartan treatment to lower end diastolic velocity (**J**) and increase arterial resistive index (**K**) of ion-poor-treated larvae. Peak systolic velocity appeared unaffected by both treatment times (**I**).  $n_{\text{control}} = 11$  larvae,  $n_{\text{ion-poor}} = 15$  larvae,  $n_{\text{ion-poor, early losartan}} = 13$  larvae,  $n_{\text{ion-poor, late losartan}} = 9$  larvae. Results in bar graphs are presented as mean  $\pm$  S.E.M. Individual data points are also shown as dot plots. \* $P < 0.05$ , \*\* $P < 0.01$ , \*\*\* $P < 0.001$ , n.s. not significant, t-test. *P* values were adjusted for multiple comparisons.

pathway. However, one or more additional disease drivers may take part subsequently in the pathogenic cascade, rendering RAS antagonism ineffective at later stages.

### 3.3 Ion imbalance leads to cardiomyocyte hypertrophy and ventricular diastolic dysfunction

Next, we examined whether the ion-poor-induction of high arterial pressure is sufficient to drive cardiovascular complications most frequently associated with hypertension. Indeed, following the 5-day ion-poor treatment, larvae displayed decreased ability of ventricular relaxation as evidenced by slower movement of the ventricular wall in diastole (Figure 2A and B and see Supplementary material online, Movies S1 and S2). On the contrary, systolic velocity in these hearts was unaltered (Figure 2C and see Supplementary material online, Movies S1 and S2).

Preserved systolic functionality was also shown by unimpaired ejection fraction (Figure 2D) and fractional shortening (Figure 2E).

Functional impairments of the heart are a consequence of maladaptive morphological remodelling of the myocardium. To examine possible cellular alterations of cardiomyocytes as a consequence of the ion-poor induction of arterial hypertension, we applied the ion-poor treatment paradigm to *myl7:H2B-GFP*; *myl7:mKATE-CAAX* transgenic larvae in which cardiomyocyte nuclei and plasma membranes were fluorescently labelled with H2B-GFP and mKATE-CAAX, respectively. Analysis of cardiomyocyte size showed an increase of cell volume in ion-poor treated ventricles (Figure 2F and G), indicating hypertrophic growth. Myocardial cell death is often associated with cardiac diseases and, to some extent, can occur in the hypertrophic heart.<sup>28</sup> Therefore, we examined whether reduction of cardiomyocyte number could contribute to the dysfunction of mechanical relaxation. However, ion-poor treated ventricles contained similar numbers of cardiomyocytes as in control siblings (Figure 2H and I). Ventricular volume was also unaffected (Figure 2J and K), suggesting the

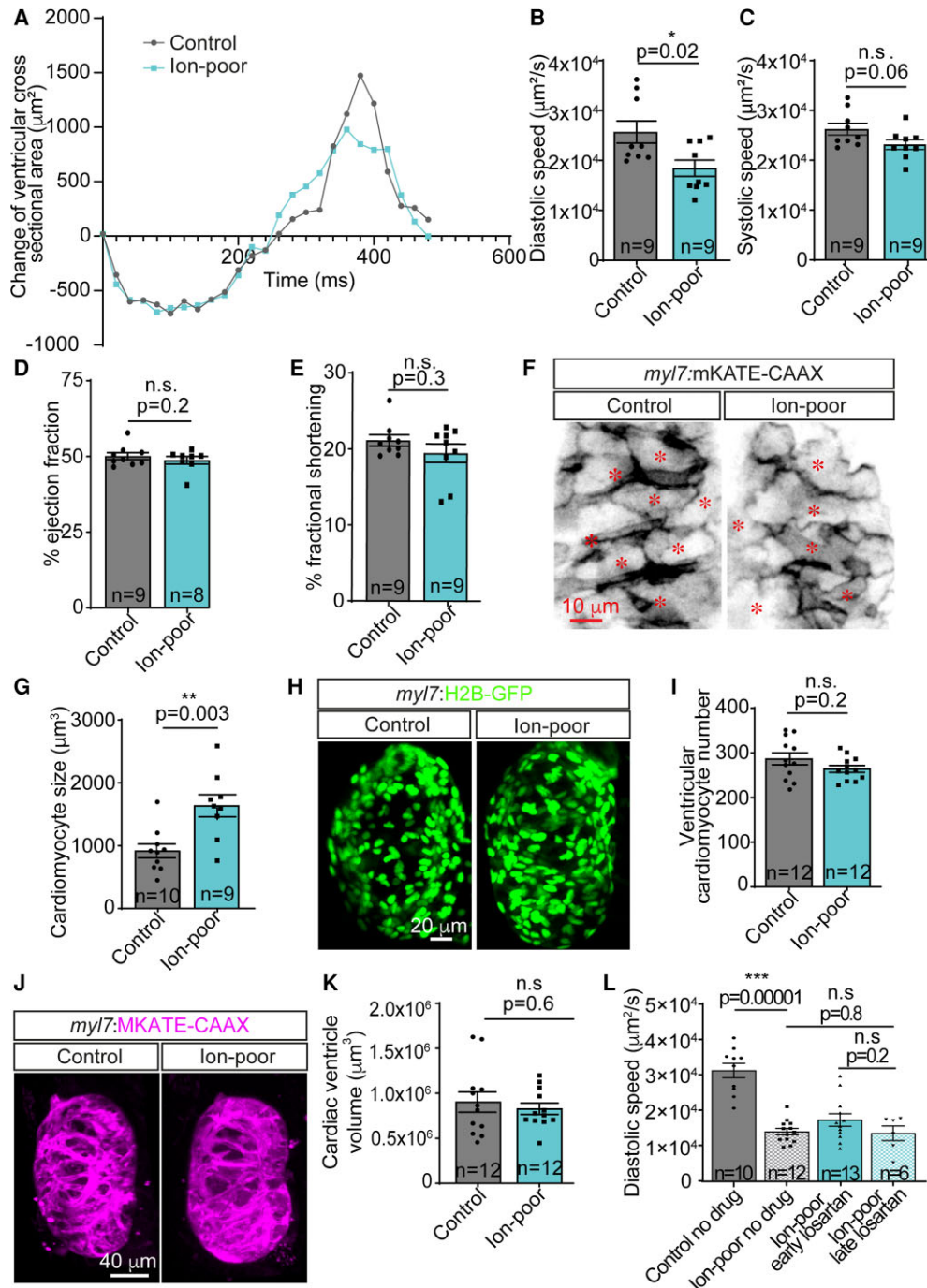


**Figure 2** RAS-independent diastolic dysfunctional remodelling of the ventricle in the ion imbalance zebrafish model. **A**, Line graph depicting changes of ventricular area of a control and an ion-poor-treated larva over time. **B–E**, Bar graphs showing reduction of ventricular wall velocity in diastole (**B**,  $n_{\text{control}} = 9$  larvae,  $n_{\text{ion-poor}} = 9$  larvae) but unaffected systolic function (**C**,  $n_{\text{control}} = 9$  larvae,  $n_{\text{ion-poor}} = 9$  larvae; **D**,  $n_{\text{control}} = 9$  larvae,  $n_{\text{ion-poor}} = 8$  larvae; **E**,  $n_{\text{control}} = 9$  larvae,  $n_{\text{ion-poor}} = 9$  larvae) in zebrafish larvae exposed to 5 days ion-poor treatment. Data are associated with representative [Supplementary material online, Movies S1 and S2](#), showing myocardial movement in systole and diastole. **F**, Enlargement of cardiomyocytes in the compact layer of the ventricular wall, labelled by *mKATE-CAAX* in the plasma membrane, following 5-day ion-poor treatment. Asterisks mark individual cardiomyocytes. **G**, Bar graph depicting cardiomyocyte volume of control and ion-poor-treated siblings.  $n_{\text{control}} = 10$  larvae,  $n_{\text{ion-poor}} = 9$  larvae. **H**, *Tg(my17:H2B-GFP)* larval hearts reared in control condition and in ion-poor condition for 5 days. Cardiomyocytes were detectable by the presence of nuclear H2B-GFP. **I**, Bar graph presenting comparable numbers of cardiomyocytes in the ventricle of control and ion-poor-treated siblings.  $n_{\text{control}} = 12$  larvae,  $n_{\text{ion-poor}} = 12$  larvae. **J**, 3D projection of *Tg(my17:mKATE-CAAX)* cardiac ventricle showing unchanged size upon 5 days ion-poor treatment. **K**, Bar graph displaying ventricular volume in control and ion-poor-treated siblings.  $n_{\text{control}} = 12$  larvae,  $n_{\text{ion-poor}} = 12$  larvae. **L**, Bar graph showing similar extent of diastolic dysfunction when RAS activity is blocked with losartan during early or late stage of ion-poor treatment.  $n_{\text{control}} = 10$  larvae,  $n_{\text{ion-poor, no drug}} = 12$  larvae,  $n_{\text{ion-poor, early losartan}} = 13$  larvae,  $n_{\text{ion-poor, late losartan}} = 6$  larvae. Results in bar graphs are presented as mean  $\pm$  S.E.M. Individual data points are also shown on top of the bar graphs. \* $P < 0.05$ , \*\* $P < 0.01$ , \*\*\* $P < 0.001$ , n.s. not significant, *t*-test. *P* values were adjusted for multiple comparisons.

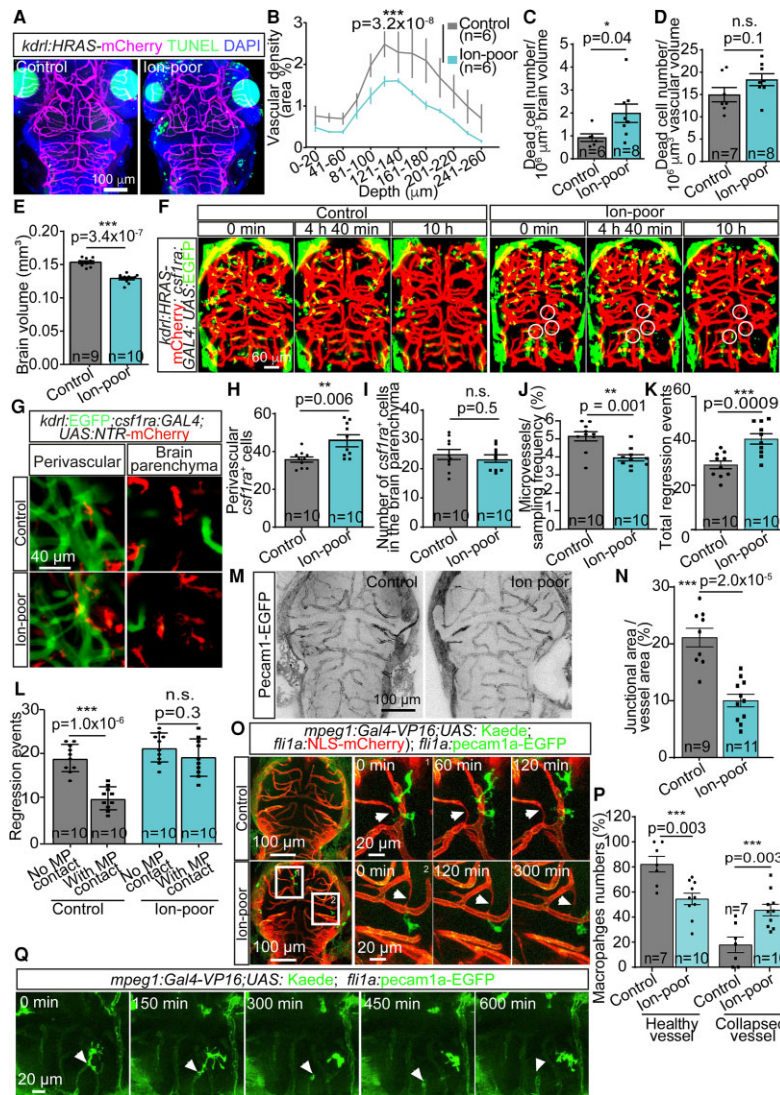


**Figure 3** Ion imbalance-driven cerebrovascular regression and brain cell death are associated with increased macrophage/microglia-endothelial cell contacts and inter-endothelial junctional remodelling. **A**, Structural remodelling of the hypertensive brain. Cerebrovascular morphology and cell death (TUNEL+) were assessed in 5 dpf *Tg(kdr:HRAS-mCherry)* larvae exposed to ion-poor treatment for 3 days. 4',6-diamidino-2-phenylindole (DAPI, blue) labelled all nuclei in the tissue. **B**, Line graph depicting 3-day ion-poor induced reduction of vascular density (expressed as percentages of total tissue area) throughout the brain parenchyma.  $n_{\text{control}} = 6$  larvae,  $n_{\text{ion-poor}} = 6$  larvae. **C–E**, Bar graphs showing an increase of cell death in the brain parenchyma (**C**,  $n_{\text{control}} = 6$  larvae,  $n_{\text{ion-poor}} = 8$  larvae) but not in the cerebral vessels (**D**,  $n_{\text{control}} = 7$  larvae,  $n_{\text{ion-poor}} = 8$  larvae) at 3 days of ion-poor treatment (expressed as number of TUNEL+ cell per  $10^6 \mu$ m tissue volume), and subsequent reduction of brain volume (**E**,  $n_{\text{control}} = 9$  larvae,  $n_{\text{ion-poor}} = 10$  larvae) at 5 days of the treatment, as compared to control siblings. **F**, Time-lapse imaging of *kdr:HRAS-mCherry; csf1ra:GAL4; UAS:EGFP* transgenic zebrafish to trace dynamic changes of endothelial cells and macrophage/microglia behaviours in ion-poor treated and control siblings. The live imaging started at 2.5 days of the treatment. The still images shown here are selected frames of the [Supplementary material online, Movies S3 and S4](#). Circles mark locations of endothelial retraction during the course of the time series. **G**, *Csf1ra*+ macrophage/microglia (*csf1ra:GAL4; UAS:NTR-mCherry*) having direct contact and/or localized in close proximity to the vasculature (*kdr:EGFP*), or residing distantly from vessels in the brain parenchyma in 2 days ion-poor-treated animals as compared with control siblings. **H**, Bar graph displaying higher number of vessel-associated *Csf1ra*+ cells upon hypertensive response.  $n_{\text{control}} = 10$  larvae,  $n_{\text{ion-poor}} = 10$  larvae. **I**, Bar graph showing comparable parenchymal *Csf1ra*+ cell numbers in ion-poor-treated and control siblings.  $n_{\text{control}} = 10$  larvae,  $n_{\text{ion-poor}} = 10$  larvae. **J–L**, Bar graphs presenting reduction of microvessel sampling frequency (**J**) resulting from increased endothelial regression (**K**) and correlating with the loss of macrophage/microglia-endothelial contact-associated regress protection (**L**) upon ion-poor treatment.  $n_{\text{control}} = 10$  larvae,  $n_{\text{ion-poor}} = 10$  larvae. **M** and **N**, Endothelial junctional disruption upon ion-poor treatment. Reduced integrity of endothelial junction, visualized by platelet endothelial cell adhesion molecule (PECAM)-EGFP expression (**M**), is expressed as percentages of junctional coverage per vascular area (**N**).  $n_{\text{control}} = 9$  larvae,  $n_{\text{ion-poor}} = 11$  larvae. **O**, Images captured from time-lapse [Supplementary material online, Movies S5–S8](#), showing cellular interactions between endothelial cells and macrophages/microglia, endothelial cells, and endothelial junctions. **P**, Bar graph showing lower macrophage coverage of healthy vessels and higher coverage of collapsed vessel in ion-poor-treated larvae as compared to control siblings.  $n_{\text{control}} = 7$  larvae,  $n_{\text{ion-poor}} = 10$  larvae. **Q**, Images captured from time-lapse [Supplementary material online, Movie S9](#) depicting macrophage/microglia contact prior to rearrangement of inter-endothelial junction, visualized by PECAM-EGFP expression. Data are shown as mean  $\pm$  S.E.M. and individual data points are superimposed to bar graphs. \* $P < 0.05$ , \*\* $P < 0.01$ , \*\*\* $P < 0.001$ , n.s. not significant, t-test or two-way analysis of variance (**B**). *P* values were adjusted for multiple comparisons.

establishment of concentric hypertrophy. Unlike arterial flow change, RAS blockage at early or late stage of the ion-poor-induced RAS activation (Figure 1G and F) did not prevent diastolic dysfunction of the myocardium (Figure 2L). These results demonstrate that ion-poor treatment, independently of RAS, causes ventricular diastolic dysfunction associated with adaptive hypertrophic remodelling of cardiomyocytes without cardiomyocyte death, resembling certain functional and morphological hallmarks of incipient heart failure with preserved ejection fraction (HFpEF).<sup>28,29</sup>

### 3.4 Cerebrovascular regression, increased vessel-associated macrophages/microglia, and induction of cell death in the brain in response to ion imbalance

Having validated the presence of cardiovascular phenotypes and elevation of the key molecular markers of hypertension in response to ion-poor treatment, we next investigated the cellular processes underlying adverse remodelling of target organs and involvement of immune cells in the zebrafish model. As the primary contact site of infiltrated immune cells, vascular injury is often viewed as a mechanistic link between systemic inflammation and development of hypertension and its related target organ damage. Therefore, we proceeded to examine endothelial response to ion imbalance and interaction with immune cells, in particular monocytes/macrophages previously shown to play a key role in RAS-induced vascular injury.<sup>10,12</sup> We first assessed the trunk vascular bed comprising the major artery and vein, the dorsal aorta and cardinal vein, ramifying into networks of smaller vessels feeding the skeletal muscles and the peripheral nervous system. Whole mount imaging of *kdr1:HRAS-mCherry* transgenic larvae, in which endothelial cells were fluorescently labelled by the membrane-localized Harvey rat sarcoma viral oncogene homolog (HRAS)-tagged mCherry, showed no overt morphological alteration of the vascular network after 3 days of ion-poor treatment (see [Supplementary material online, Figure S1A](#)). Vascular density, measured as percentage of total tissue volume, was also comparable in ion-poor and control siblings (see [Supplementary material online, Figure S1B](#)). In contrast, reduction of vascular density in the ion-poor group was evident in the brain (Figure 3A and B). Vascular rarefaction occurred throughout the depth of the brain (Figure 3B) and was associated with increased parenchymal cell death, detected by terminal deoxynucleotidyl transferase 2'-Deoxyuridine, 5'-Triphosphate (dUTP) nick end labelling (TUNEL) (Figure 3A and C). Endothelial cell death was not significantly increased (Figure 3D), suggesting that apoptosis might not be a primary mechanism of ion imbalance-driven cerebral vascular rarefaction. Subsequently, after 5 days of treatment, reduction of brain volume was also detectable (Figure 3E).

Vascular regression involving endothelial cell migration and reintegration into retracted vessel segments, independently of endothelial apoptosis, was observed during developmental remodelling of different vascular beds.<sup>30,31</sup> It was previously unknown whether this cellular process takes part in hypertensive remodelling of cerebral vessels. Time-lapse imaging of *kdr1:HRAS-mCherry; csf1ra:GAL4; UAS:EGFP* transgenic larvae, in which endothelial cells (*kdr1+*) and macrophages/microglia (*csf1ra+*) were fluorescently labelled with mCherry and EGFP, respectively, showed mainly a stabilized brain vascular network in zebrafish larvae reared under control condition (see [Supplementary material online, Movie S4](#) and Figure 3F). At 4.5–5 dpf, after 2 days of ion-poor treatment, we captured a dynamic process of endothelial cells from the same vascular segments undergoing retraction and migration away from each other, leading to regression of the segments (see [Supplementary material online, Movie S4](#) and Figure 3F). Moreover, higher numbers of *csf1ra+* cells located adjacent to the vessels and only moving along the vascular fragment, were present in the ion-poor-treated group (see [Supplementary material online, Movie S3](#) and Figure 3G and H). Parenchymal *csf1ra+* cell numbers, by contrast, remained unchanged (Figure 3G and I), suggesting enhanced interactions between macrophages/microglia and the blood vessels but not expansion of all myeloid cells in the brain parenchyma.

In summary, the pathogenic pathway initiated by ion-poor-induced RAS up-regulation triggers remodelling of not only the cardiovascular system, but also the brain through a series of cellular responses of immune and non-immune cells, i.e. increased association of macrophages/microglia with the cerebral vessels, endothelial migration-mediated vascular regression, and brain parenchymal cell death. Interestingly, the ion-poor-induced endothelial regression mainly affected microvessels (diameter  $\leq 5 \mu\text{m}$ ), but not larger ones (Figure 3J) and see [Supplementary material online, Figure S1C and D](#)). Moreover, prolonged ion-poor treatment for 8 days showed progression of cerebrovascular rarefaction, as seen from further reduction of vascular density (see [Supplementary material online, Figure S2A and B](#)), but no overt morphological abnormality, with the exception of the primitive kidney, the pronephros (see [Supplementary material online, Figure S2C](#)). Thus, system-wide response triggered by ion imbalance recapitulates damage of the blood vessel, heart, brain, and kidney, all prime target organs of human hypertension.

### 3.5 Endothelial-macrophage/microglia cellular interactions and endothelial junctional disruption in ion imbalance-induced cerebrovascular retraction

Next, we aimed to gain further insight into the cellular mechanism underlying regression of the cerebral vessels observed in the ion-poor-treated animals. Surprisingly, while analysis of the relationship between macrophage/microglia-endothelial interactions and vascular regression revealed more frequent regressions in the ion-poor-treated as compared to siblings (Figure 3K), contact with macrophage/microglia correlated with fewer regression events under control condition (Figure 3L), implying a protective role of the innate immune cells. By contrast, upon ion imbalance, comparable regression events of vascular segments with and without prior cellular contact with macrophage/microglia suggested loss of the protective effect (Figure 3L). Perivascular macrophages have been reported to contribute to increased BBB permeability that is linked to reduction of endothelial tight junction complexity in hypertension.<sup>32</sup> To assess whether ion-poor treatment affects cellular configuration in cerebral microvessels, we measured junctional coverage as an estimate for cell contact area in treated and non-treated larvae. Examination of intercellular junctions, visualized by localization of platelet endothelial cell adhesion molecule-1 (Pecam1) using the transgenic reporter line *fli1a:pecam1a-EGFP*, showed reduced junctional coverage along the brain vascular network upon ion-poor treatment (Figure 3M and N). To elucidate the involvement of macrophage/microglia in endothelial junctional remodelling and regression, we traced macrophage/microglia making contact with perfused/or inflated vs. collapsed vascular segments by time-lapse imaging of the *mpeg:GAL4-VP16; UAS:Kaede; kdr1:HsHRAS-mCherry; fli1a:pecam1a-EGFP* transgenic line, in which macrophages/microglia, endothelial cells, and endothelial junction were visualized by Kaede, mCherry, and EGFP expression, respectively (Figure 3O and see [Supplementary material online, Movies S5–S8](#)). In addition to capturing the endothelial-macrophage/microglia interactions preceding retraction (Figure 3O and see [Supplementary material online, Movie S8](#)) and reestablishment of vascular segments (Figure 3O and see [Supplementary material online, Movie S7](#)), our analysis revealed that ion-poor treatment alters the distribution of macrophages/microglia along the vascular network. Under control condition, majority of vessel-associated macrophages/microglia were in contact with perfused/inflated vessels. Only a few macrophages/microglia were associated with the regression events, which occurred as part of physiological maturation of the vascular bed (Figure 3P). Ion-poor treatment did not have major impact on macrophage/microglia coverage of perfused vessels, but augmented their interaction with collapsed vessels (Figure 3P). Moreover, inter-endothelial junctional regression following macrophage/microglia contact was noticeable in ion-poor-treated brains (Figure 3Q and see [Supplementary material online, Movie S9](#)). Collectively, using time-lapse tracing of macrophages/

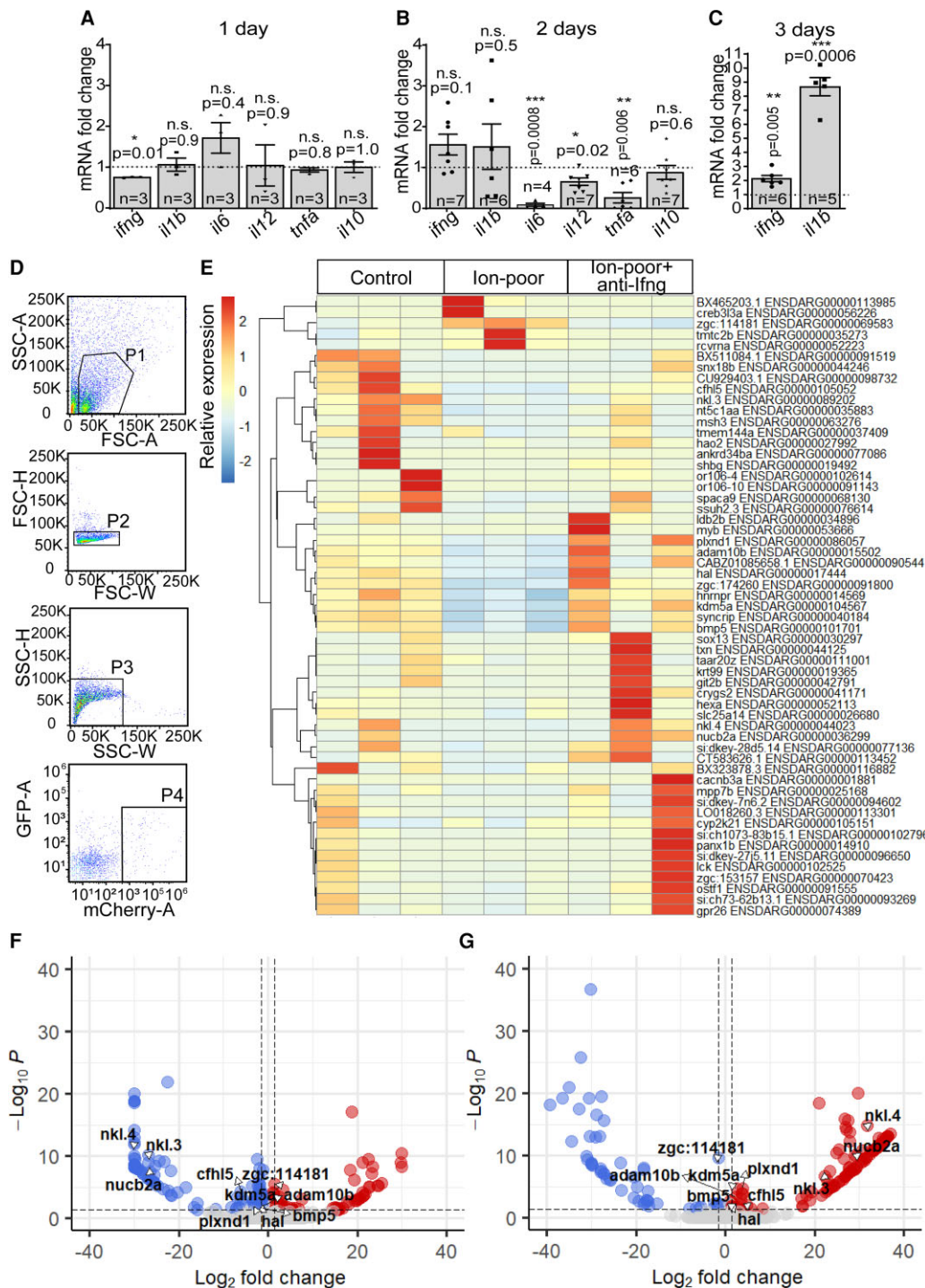


**Figure 4** Systemic inflammation characterized by *ifng* and *il1b* up-regulation and *lfnr* signalling-dependent down-regulation of neuroprotective and homeostatic gene expression in macrophages in response to hypertensive stimulus. **A**, Unaltered expression of cytokines reported to be involved in hypertension and HFpEF at 1 day of ion-poor treatment.  $n = 3$  biological replicas (pooled larvae) per group. **B** and **C**, Progressive elevation of the pro-inflammatory/Th1 cytokines *ifng* and *il1b* mRNA levels detected after 2 days (**B**,  $n_{ifng} = 7$  biological replicas,  $n_{il1b} = 6$  biological replicas,  $n_{il6} = 4$  biological replicas,  $n_{il12} = 7$  biological replicas,  $n_{tnfa} = 6$  biological replicas,  $n_{il10} = 7$  biological replicas) and 3 days (**C**,  $n_{ifng} = 6$  biological replicas,  $n_{il1b} = 5$  biological replicas) of ion-poor treatment. Bar graphs show mean  $\pm$  S.E.M. Individual data points are shown superimposed to the bar graphs. \* $P < 0.05$ , \*\* $P < 0.01$ , \*\*\* $P < 0.001$ , *n.s.* not significant, *t*-test. *P* values were adjusted for multiple comparisons. *n* indicates number of biological replicas (pooled larvae). **D**, Isolation of macrophages from control larvae injected with anti-V5 (control), 3-day ion-poor-treated larvae injected with anti-V5 (ion-poor), and 3-day ion-poor-treated larvae injected with anti-*lfnr* (ion-poor + anti-*lfnr*) by FACS before subjecting them to RNA-Seq. **E**, Heatmap depicting differentially expressed genes (adjusted *P*-value  $< 0.05$ ) in control, hypertensive, and anti-*lfnr*-treated hypertensive macrophages. **F** and **G**, Volcano plots showing up-regulated (positive  $\text{Log}_2$  fold change) and down-regulated (negative  $\text{Log}_2$  fold change) genes in ion-poor as compared to control macrophages (**F**) and ion-poor + anti-*lfnr* as compared to ion-poor-treated macrophages. Grey dots indicate genes not differentially expressed. Data in (**D**–**G**) were obtained from three biological replicas per group.



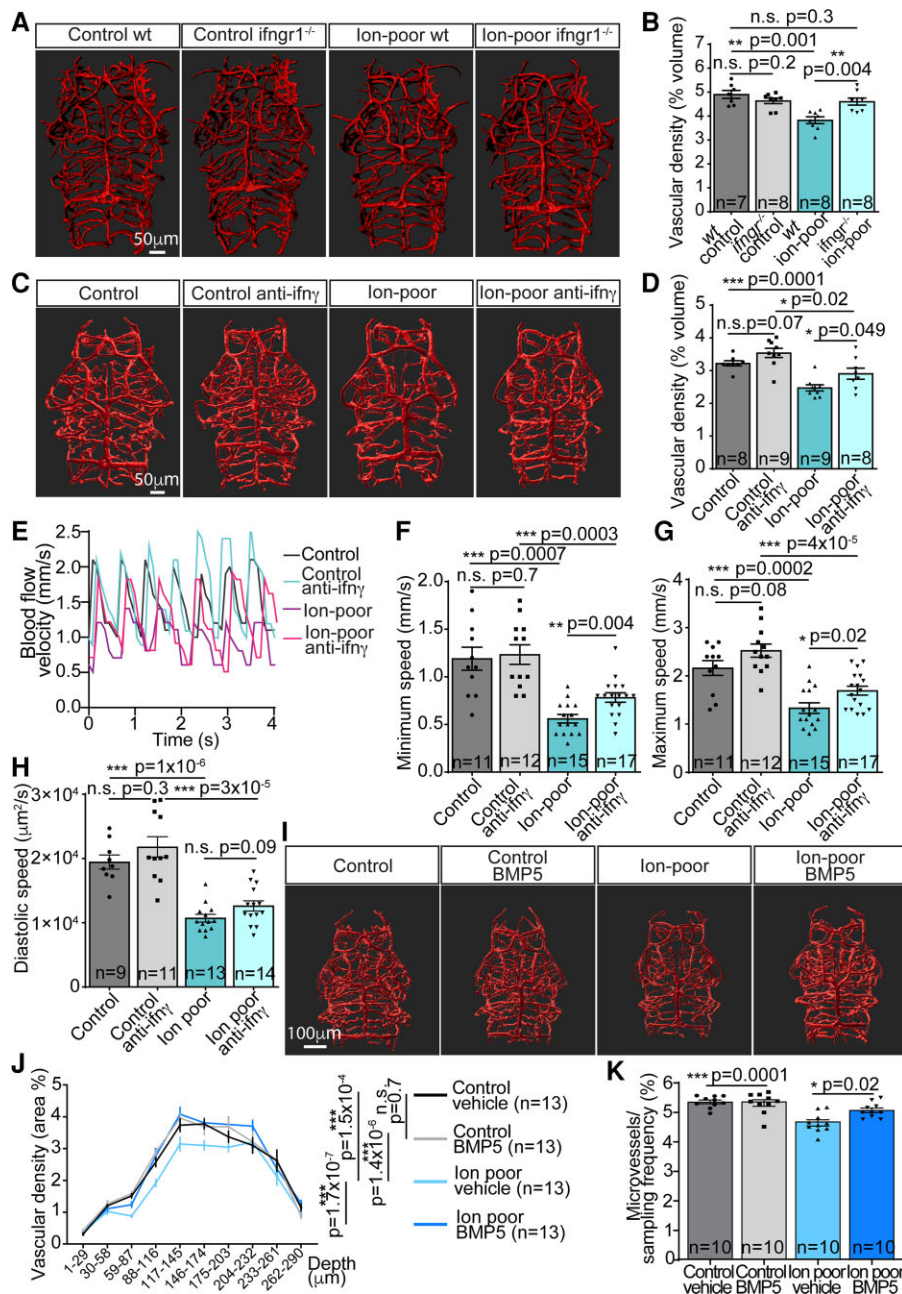


**Figure 5** *Ifn* $\gamma$  and its downstream signalling target *Bmp5* regulate vascular response to the ion imbalance hypertensive stimulus. **A**, Representative images showing brain vasculature of 5 dpf *ifngr1*<sup>-/-</sup> and control wild type *Tg(kdrl:HRAS-mCherry)* larvae exposed or not to ion-poor treatment for 3 days. **B**, Bar graph showing vascular volume (expressed as percentages of total tissue volume) of wild-type controls, *ifngr1*<sup>-/-</sup>, ion-poor-treated wild type, and ion-poor-treated *ifngr1*<sup>-/-</sup> siblings.  $n_{wt, control} = 7$  larvae,  $n_{ifngr1^{-/-}, control} = 8$  larvae,  $n_{wt, ion-poor} = 8$  larvae,  $n_{ifngr1^{-/-}, ion-poor} = 8$  larvae. **C**, Brain vasculature of *Tg(kdrl:HRAS-mCherry)* larvae exposed or not to ion-poor treatment for 5 days. A single dose of anti-*Ifn* $\gamma$  administration after the manifestation of cerebrovascular rarefaction at 3 days of ion-poor treatment partially restored the phenotype, measured at 5 days of the treatment. **D**, Bar graph displaying vascular volume (expressed as percentages of total tissue volume) of control antibody (anti-V5)-injected (control), anti-*Ifn* $\gamma$  injected, ion-poor-treated anti-V5 injected (ion poor), and ion-poor-treated anti-*Ifn* $\gamma$  injected samples.  $n_{control} = 8$  larvae,  $n_{control, anti-ifn\gamma} = 9$  larvae,  $n_{ion-poor} = 9$  larvae,  $n_{ion-poor, anti-ifn\gamma} = 8$  larvae. **E**, Line graphs depicting time course of blood flow velocities of representative anti-V5-injected (control), anti-*Ifn* $\gamma$ -injected, anti-V5-injected ion-poor (ion-poor) treated, and anti-*Ifn* $\gamma$ -injected ion-poor-treated larvae. **F**, Bar graphs showing improvement of end diastolic velocity ( $n_{control} = 11$  larvae,  $n_{control, anti-ifn\gamma} = 12$  larvae,  $n_{ion-poor} = 15$  larvae,  $n_{ion-poor, anti-ifn\gamma} = 17$  larvae) and **G**, peak systolic velocity by anti-*Ifn* $\gamma$  administration ( $n_{control} = 11$  larvae,  $n_{control, anti-ifn\gamma} = 12$  larvae,  $n_{ion-poor} = 15$  larvae,  $n_{ion-poor, anti-ifn\gamma} = 17$  larvae). **H**, Ventricular diastolic dysfunction was not altered by anti-*Ifn* $\gamma$  treatment. ( $n_{control} = 9$  larvae,  $n_{control, anti-ifn\gamma} = 11$  larvae,  $n_{ion-poor} = 13$  larvae,  $n_{ion-poor, anti-ifn\gamma} = 14$  larvae). **I–K**, Treatment with human recombinant *BMP5* prevented cerebrovascular regression in ion-poor-induced hypertension. Brain vasculature of *Tg(kdrl:HRAS-mCherry)* larvae treated for 2 days with *BMP5* starting at the second day of ion-poor exposure (**I**) exhibiting increased density (**J**) and microvessel sampling frequency (**K**) as compared to ion-poor exposed siblings treated with vehicle.  $n = 13$  and 10 larvae for all treatment groups in **J** and **K**, respectively. Graphs represent mean  $\pm$  S.E.M. Individual data points are also shown superimposed to bar graphs. \* $P < 0.05$ , \*\* $P < 0.01$ , \*\*\* $P < 0.001$ , n.s. not significant, *t*-test, or two-way analysis of variance (**J**). *P* values were adjusted for multiple comparisons.

microglia and endothelial cellular behaviours not only unveiled a role of ion imbalance in the dynamic interactions among these cells, but also indicates a cellular mechanism through which alteration of macrophages/microglia vasculoprotective function may lead to microvascular retraction. Moreover, our observations on junctional dynamics suggest a cellular mechanism which is consistent with previous *in vivo* studies on vascular pruning.<sup>33</sup>

### 3.6 Ion imbalance up-regulates the pro-inflammatory cytokines *Ifn $\gamma$* and *IL1 $\beta$* and skews macrophage tissue homeostatic/neuroprotective phenotype via *Ifn $\gamma$* signalling

To address the role of inflammation as a subsequent driver of the ion imbalance signalling succeeding RAS dysregulation and to identify the immune pathway mediating its damaging effects on target organs, we first probed the temporal relationship between the development of cardiovascular phenotypes and expression levels of inflammatory markers commonly associated with hypertension and HFpEF.<sup>34–36</sup> At 1 day of the ion-poor treatment, qRT–PCR showed no alteration of candidate cytokine expression as compared to control siblings (Figure 4A). After 2 days of treatment, a subtle increase (approximately 1.5 folds) in the expression levels of two cytokines, *ifng* and *il1b*, became noticeable, but not statistically significant (Figure 4B). Subsequent assessment at 3 days of treatment showed over 2-fold and 8-fold up-regulation of *ifng* and *il1b* mRNA, respectively (Figure 4C). This elevation of the two pro-inflammatory cytokines suggests that systemic inflammation, possibly resulting from RAS dysregulation, contributes to the ion-poor-induced pathogenic pathway.

IFN $\gamma$  is a benchmark stimulus for activation of a macrophage subset highly potent in pro-inflammatory cytokine production and microbicidal activity.<sup>37</sup> IL1 $\beta$  is one of the key cytokines up-regulated by IFN $\gamma$ -primed macrophages.<sup>38</sup> We hypothesized that phenotypic alteration and thereby derangement of macrophage/microglia vasculoprotective function, as a result of *Ifn $\gamma$*  elevation, contributes to cerebral vessel regression and brain cell death. To address this hypothesis and gaining an understanding of the downstream signalling, we conducted RNA-Seq of monocytes/macrophages isolated by Fluorescent-Activated Cell Sorting (FACS) from control and ion-poor *csf1ra:GAL4; UAS:NTR-mCherry* larvae, subjected to 3-day ion-poor exposure and intrapericardial injection of control V5 or anti-*Ifn $\gamma$*  antibody to block interferon gamma receptor (*Ifngr*) 1 activation after a day of the treatment (Figure 4D). Comparative transcriptomic analysis revealed not only disruption of innate immunity function, but also blunted expression of several critical mediators of inflammatory resolution and tissue homeostatic maintenance in response to ion imbalance (Figure 4E and F). Specifically, ion-poor-treated macrophages down-regulated the complement system regulator complement factor H related 5 (*cfhl5*), and bactericidal and innate immune effector peptides natural killer (NK)-lysin (*nkl.3* and *nkl.4*)<sup>39,40</sup> (Figure 4E and F). Expression of different enzymes involved in anti-inflammatory response and resolution of inflammation such as A disintegrin and metalloproteinase domain 10b (*adam10b*), histidine ammonia-lyase (*hal*), and lysine demethylase 5A (*kdm5a*)<sup>41–43</sup> were also reduced (Figure 4E and F). Intriguingly, we observed upon exposure to the ion imbalance transcriptional suppression of secreted factors and cell surface receptors, including *bmp5*, nucleobindin 2a (*nucb2a*), and plexin D1 (*plxnd1*) (Figure 4E and F), reported to play important roles in neuronal and vascular homeostasis and damage prevention in different pathological settings.<sup>44–49</sup> Importantly, anti-*Ifn $\gamma$* -mediated inhibition of the intrinsic cytokine signalling prevented activation of the ion-poor-driven transcriptional programme (Figure 4E and G), indicating that *Ifn $\gamma$*  signalling is a crucial mediator of phenotypic alteration of macrophage in ion imbalance response. From our transcriptomic analysis we also noticed that, unlike its cognate receptor *ifngr1*, *ifng* expression was not detectable in macrophages. IFN $\gamma$  is a signature cytokine associated with hypertensive response in T cells.<sup>9</sup> Intriguingly, ion-poor-treated fish, showed accumulation of T

cells within the vicinity of the brain, which was rarely observed in control animals (see Supplementary material online, Figure S3), suggesting involvement of these cells in macrophage dysregulation.

### 3.7 *Ifn $\gamma$* signalling underlies ion imbalance-driven cerebrovascular regression

Next, we examined a possible causal role of *Ifn $\gamma$*  signalling in ion imbalance-driven cerebrovascular remodelling employing a genetic loss-of-function model: zebrafish larvae harbouring a nonsense mutation in the gene encoding the *ifngr1*.<sup>50</sup> In the absence of the ion imbalance stimulus, *ifngr1*<sup>-/-</sup> larvae showed comparable cerebrovascular morphology and density to control siblings (*ifngr1*<sup>+/+</sup>) (Figure 5A and B). By comparison, exposure to ion-poor medium led to a reduction of vessel density measured in the brain at 3 days of the treatment (Figure 5A and B). *Ifngr1* deficiency protected cerebral vessels from ion-poor-mediated regression (Figure 5A and B), indicating that *Ifn $\gamma$*  signalling plays a critical role in the pathogenic response of the brain vasculature to ion imbalance. Hence, we proceeded to address if the cytokine may represent a therapeutic target capable of preventing and/or alleviating end organ damage after the progression of phenotypic manifestations.

To this end, we administered anti-*Ifn $\gamma$*  antibody with a single-dose intrapericardial injection during the continuous 5-day ion-poor exposure after arterial hypertension and cerebrovascular rarefaction became detectable (at 3 days of treatment). The anti-*Ifn $\gamma$*  treatment paradigm was capable of attenuating cerebrovascular rarefaction (Figure 5C and D). Interestingly, late anti-*Ifn $\gamma$*  antibody treatment also mitigated the ion-poor-induced reduction of arterial flow velocity in both systole and diastole (Figure 5E–G). The treatment, however, did not restore the diastolic dysfunction, measured by ventricular wall velocity in diastole (Figure 5H).

Collectively, these findings unravel a mechanism of inflammatory-driven pathogenesis of hypertension in which the aberrant production of *Ifn $\gamma$*  drives brain remodelling, characterized by cerebrovascular regression and increased brain cell death. Interfering with activation of the *Ifn $\gamma$*  pathway alleviates vascular damage, and arterial hypertension, but is insufficient to prevent the progression of cardiac remodelling.

### 3.8 BMP5 supplementation prevents ion imbalance-driven cerebrovascular rarefaction

Macrophage/microglia transcriptomic alteration and functional dysregulation, as evidenced from their contact-associated endothelial regression upon ion imbalance challenge, suggest that *Ifn $\gamma$* -mediated impairment of macrophage paracrine signalling may be an underlying mechanism mediating brain vascular remodelling. Remarkably, we found that a downstream target of *Ifn $\gamma$* -mediated transcriptional down-regulation in macrophages/microglia, identified from the transcriptomic analysis, BMP5, is an important modulator of ion imbalance-driven cerebrovascular rarefaction. Two-day treatment of zebrafish larvae with recombinant human BMP5 starting on the second day of ion-poor exposure prevented the progression of cerebrovascular rarefaction, as shown by preservation of both overall vascular coverage of the brain parenchyma (Figure 5J) and percentage of microvessels in the vascular network (Figure 5K). Our findings together thus provide further mechanistic insight into an ion imbalance-triggered inflammatory pathway driving brain damage, in which elevation of *Ifn $\gamma$*  signals down-regulation of *bmp5* in macrophage/microglia, leading to impairment of vascular homeostatic function of these cells and thereby disruption of endothelial intercellular junction and retraction.

### 3.9 Anti-IFN $\gamma$ treatment precludes cortical capillaries rarefaction and BBB disruption in mice subjected to pressure overload

Next, we further examined the role of IFN $\gamma$  signalling uncovered here in zebrafish in hypertensive damage of the mammalian brain, and assessed efficacy of anti-IFN $\gamma$  treatment to alleviate adverse cerebrovascular

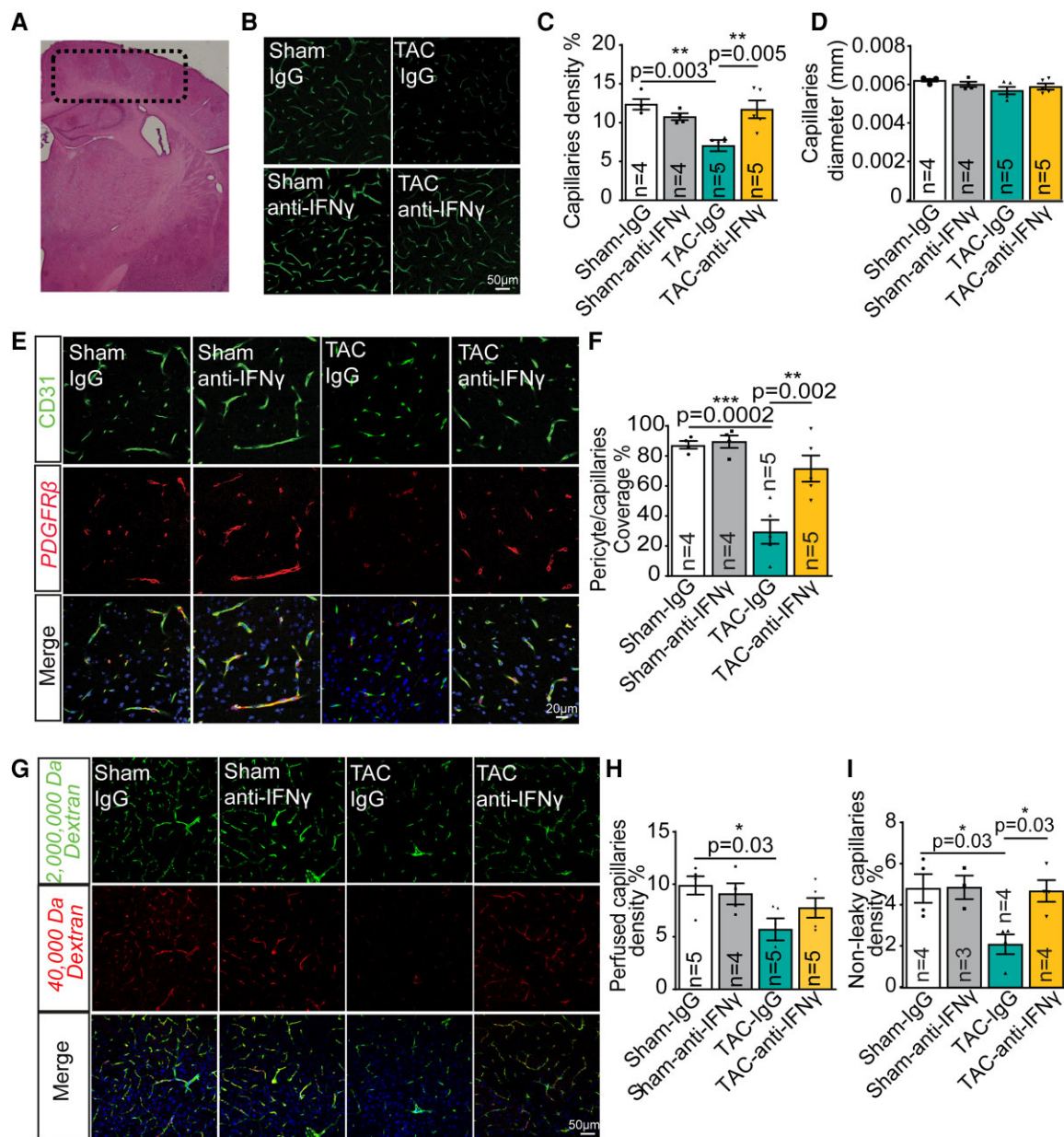


**Figure 6** IFN $\gamma$  inhibition mitigates adverse remodelling of the cerebral vasculature in a murine model of pressure overload-induced brain injury. **A**, Image showing haematoxylin and eosin staining of a coronal section of a mouse brain. The dashed rectangle indicates the cortex area used for histological analyses. **B**, Representative images of CD31 stained capillaries used to perform capillaries morphological and density analyses. **C**, Capillary density, expressed as percentage of stained vessels per Field-Of-View, was significantly reduced in mice subjected to TAC and treated with a non-relevant IgG, as compared with their Sham controls. TAC mice treated with anti-IFN $\gamma$  antibody were protected from brain capillary rarefaction.  $n_{\text{sham-IgG}} = 4$  mice,  $n_{\text{sham-anti-IFN}\gamma} = 4$  mice,  $n_{\text{TAC-IgG}} = 5$  mice,  $n_{\text{TAC-anti-IFN}\gamma} = 5$  mice. **D**, TAC-induced chronic hypertension had no effect on capillary diameter.  $n_{\text{sham-IgG}} = 4$  mice,  $n_{\text{sham-anti-IFN}\gamma} = 4$  mice,  $n_{\text{TAC-IgG}} = 5$  mice,  $n_{\text{TAC-anti-IFN}\gamma} = 5$  mice. **E**, Representative images of CD31/platelet-derived growth factor receptor (PDGFR)  $\beta$  stained capillaries used to analyse the pericyte-capillary coverage. **F**, TAC hypertensive mice treated with a non-relevant IgG showed a marked and significant reduction in pericyte coverage of brain capillaries, when compared with Sham controls. The anti-IFN $\gamma$  treatment protected mice from pressure overload-induced pericyte loss on brain capillaries.  $n_{\text{sham-IgG}} = 4$  mice,  $n_{\text{sham-anti-IFN}\gamma} = 4$  mice,  $n_{\text{TAC-IgG}} = 5$  mice,  $n_{\text{TAC-anti-IFN}\gamma} = 5$  mice. **G**, Representative images of cerebral capillaries from mice perfused with a mixture of high (2,000,000 Daltons (Da)) and low (40,000 Da) molecular weight dextrans, used to analyse density of perfused functional capillaries. **H**, Density of perfused capillaries expressed as percentage of vessels area per field of view was significantly reduced in mice subjected to TAC and treated with the non-relevant IgG, as compared with their Sham controls. The anti-IFN $\gamma$  treatment protected TAC mice from brain vascular rarefaction.  $n_{\text{sham-IgG}} = 5$  mice,  $n_{\text{sham-anti-IFN}\gamma} = 4$  mice,  $n_{\text{TAC-IgG}} = 5$  mice,  $n_{\text{TAC-anti-IFN}\gamma} = 5$  mice. **I**, Density of capillaries labelled by low molecular weight dextran, indicating the percentage of leaky vessels per field of view. TAC hypertensive mice treated with a non-relevant IgG had significantly impaired dextran retention, as compared with their Sham normotensive controls and to TAC mice treated with the anti-IFN $\gamma$  antibody.  $n_{\text{sham-IgG}} = 4$  mice,  $n_{\text{sham-anti-IFN}\gamma} = 3$  mice,  $n_{\text{TAC-IgG}} = 4$  mice,  $n_{\text{TAC-anti-IFN}\gamma} = 4$  mice. Data are shown as mean  $\pm$  S.E.M. Individual data points are also shown as dot plots. \* $P < 0.05$ , \*\* $P < 0.01$ , \*\*\* $P < 0.001$  indicate comparisons between groups. Two-way analysis of variance.  $P$  values were adjusted for multiple comparisons.

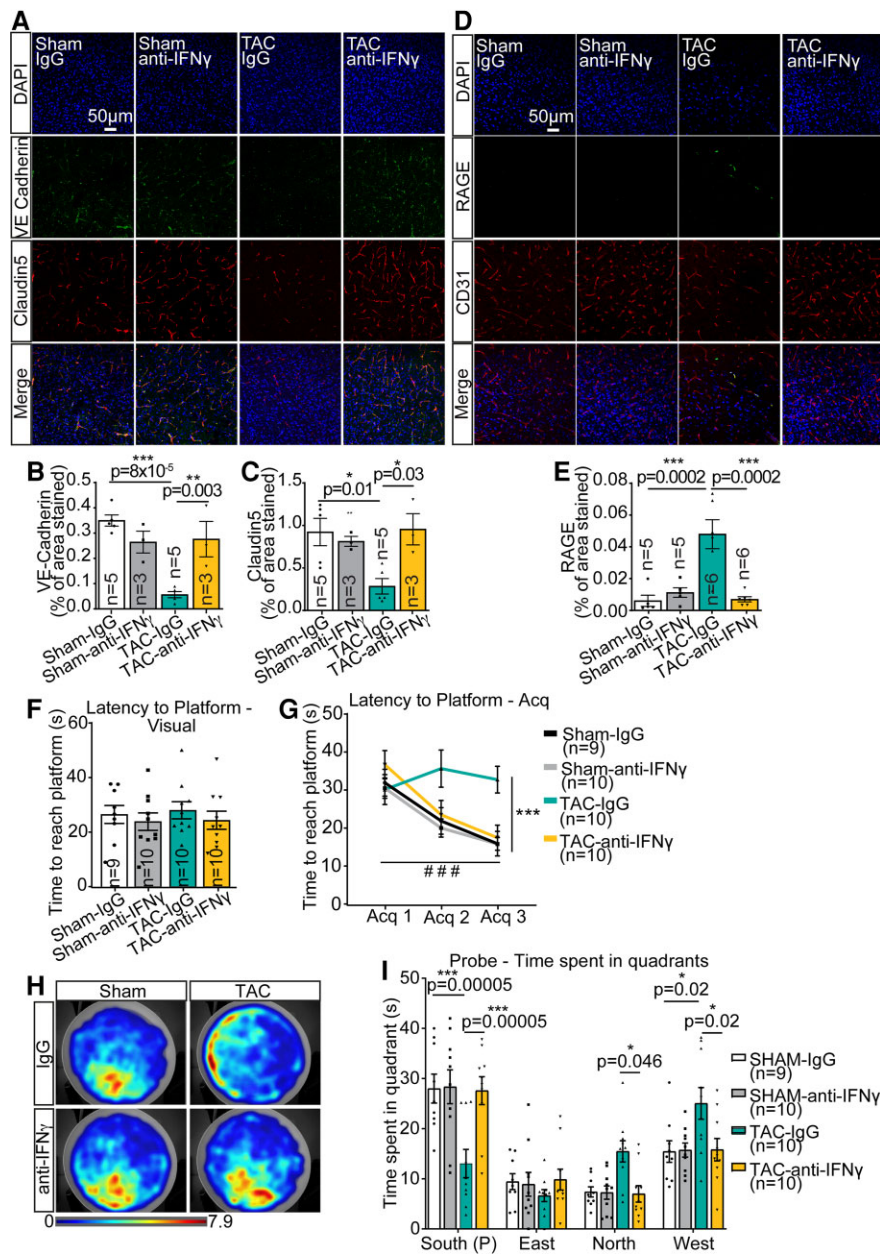


**Figure 7** Prevention of pressure overload-triggered disruption of endothelial junctional integrity and cognitive decline by anti-IFN $\gamma$  treatment. A–C, TAC mice showed a reduction of adherens and tight junction proteins vascular endothelial (VE)-Cadherin and Claudin5, an effect prevented by anti-IFN $\gamma$  neutralization. A, Representative images of VE-Cadherin and Claudin5 staining of brain capillaries, visualized by CD31. Expression levels of VE-Cadherin (B) and Claudin5 (C) are shown as percentages of area stained.  $n_{\text{sham-IgG}} = 5$  mice,  $n_{\text{sham-anti-IFN}\gamma} = 3$  mice,  $n_{\text{TAC-IgG}} = 5$  mice,  $n_{\text{TAC-anti-IFN}\gamma} = 3$  mice. D–E, anti-IFN $\gamma$  treatment mitigated the elevation of the receptor for RAGEs expression in TAC capillaries. D, Representative images of RAGE staining of CD31 + brain capillaries. E, RAGE expression levels are displayed as percentages of area stained.  $n_{\text{sham-IgG}} = 5$  mice,  $n_{\text{sham-anti-IFN}\gamma} = 5$  mice,  $n_{\text{TAC-IgG}} = 6$  mice,  $n_{\text{TAC-anti-IFN}\gamma} = 6$  mice. F, Graph showing average times to reach the platform during the Visual Trial of the Morris Water Maze test. All the mice showed similar visual acuteness and capability to identify the platform when highlighted by a visual cue. G, During the Acquisition Trial, TAC mice treated with a non-relevant antibody displayed latencies to find the platform indicative of a significantly impaired learning curve, as compared with Sham mice. TAC hypertensive mice treated with the anti-IFN $\gamma$  antibody were protected from learning deficit. H, Heatmaps of the Probe Trial, showing the preferred swimming location for each group of mice. Heatmaps are obtained by averaging the swimming time spent in each point among mice of the same experimental group. In red are the regions where mice spent more time, in blue the regions where mice spent less swimming time. The scale bar represents the quantification of the cumulative time spent in each point of the field of view, ranging from not visited points (low score) to preferred points (high score). I, At the Probe Trial, TAC mice treated with a non-relevant IgG were unable of recall the spatial location of the platform, spending time randomly in all the quadrants. The anti-IFN $\gamma$  treatment protected TAC mice from the memory deficit, as shown by the significantly higher time spent in the quadrant where the platform was located before. Results are presented as mean  $\pm$  S.E.M. Individual data points are also shown as dot plots on top of the bar graphs. \* $P < 0.05$ , \*\* $P < 0.01$ , \*\*\* $P < 0.001$  indicate comparisons between groups, ### $P < 0.001$  in (G) indicates comparisons between different time points of the same group. Two-way analysis of variance.  $P$  values were adjusted for multiple comparisons.  $n$  indicates number of animals analysed. In each graph,  $n_{\text{sham-IgG}} = 9$  mice,  $n_{\text{sham-anti-IFN}\gamma} = 10$  mice,  $n_{\text{TAC-IgG}} = 10$  mice,  $n_{\text{TAC-anti-IFN}\gamma} = 10$  mice.

remodelling and cognitive impairment commonly associated with human hypertension in a mammalian model. To this end, we used the transverse aortic constriction (TAC) model, in which localized systolic hypertension causes brain parenchymal microvascular damage and reduction of learning and spatial memory.<sup>51,52</sup> We subjected C57Bl/6J mice to TAC for 4 weeks and monitored the progression of hypertensive cardiac remodelling by echocardiography. TAC induced a progressive cardiac remodelling, characterized by concentric hypertrophy and diastolic dysfunction but no loss of systolic function (see [Supplementary material online, Figure S4A–F](#)), mirroring phenotypes observed in ion-poor-treated zebrafish and resembling a typical condition of HFpEF. No effect of the anti-IFN $\gamma$  treatment was observed either in TAC mice or in the control animals (see [Supplementary material online, Figure S4A–F](#)).

*Ex-vivo* immunohistochemistry performed on cerebral cortex sections ([Figure 6A](#)) revealed a clear pattern of damage to the neurovascular unit. Structural analysis of brain capillaries highlighted a significant capillary rarefaction in TAC-IgG hypertensive mice compared to their relative sham normotensive controls, as evidenced by a reduced vascular density labelled by cluster of differentiation 31 (CD31) ([Figure 6B and C](#)), while maintaining normal diameter ([Figure 6D](#)). Moreover, TAC-IgG mice showed a significant reduction in capillary coverage by pericytes ([Figure 6E and F](#)), a typical hallmark of neurovascular unit integrity. Interestingly, the anti-IFN $\gamma$  treatment rescued the cerebrovascular defects observed in TAC mice, showing normal capillary density ([Figure 6B and C](#)) and pericyte coverage ([Figure 6E and F](#)).

To investigate the effect of high blood pressure on the functional properties of cerebral microcirculation, we infused TAC hypertensive mice and normotensive controls with different molecular weights dextrans, before culling animals for histological analysis of the brain. By using a high molecular weight dextran (2 000 000 Da) ([Figure 6G](#)), we analysed the density of perfused capillaries, further confirming that TAC induced a significant reduction as compared with their sham controls ([Figure 6H](#)). TAC mice treated with anti-IFN $\gamma$  antibody did not develop capillary rarefaction ([Figure 6H](#)). Moreover, the combined use of a low molecular weight dextran (40 000 Da) ([Figure 6G](#)), allowed us to assess the extravasation through the BBB. Typically, the 40 kDa dextran is retained by an intact BBB, but it permeates a damaged and leaky BBB. As shown in [Figure 6G–I](#), TAC-IgG mice displayed few capillaries labelled in red, indicating that they were unable to retain the low molecular weight dextran, thus indicating reduced BBB integrity. Importantly, TAC mice treated with the neutralizing anti-IFN $\gamma$  antibody showed an intact BBB, comparable to that of sham normotensive mice. BBB dysfunction in hypertension has been attributed to Ang II-induced tight junction remodelling and increased transcytosis.<sup>32</sup> The key components of endothelial junctional complexes, vascular endothelial (VE)-cadherin and Claudin5 were, in fact, both down-regulated in the cerebral cortex of TAC mice ([Figure 7A–C](#)), indicating vascular junctional remodelling. IFN $\gamma$  neutralization effectively rescued expression of these proteins ([Figure 7A–C](#)). Furthermore, anti-IFN $\gamma$  treatment diminished the TAC-induced up-regulation of the receptor for advanced glycation end product (RAGE), a primary efflux transporter mediating transcytosis of circulating amyloid- $\beta$  (A $\beta$ ) across the BBB<sup>52</sup> ([Figure 7D and E](#)), implicating its potential, in addition to junctional stabilization, for suppression of transvascular transport of the peptide into the brain, a major cause of cognitive impairment and dementia in hypertension.

Taken together these data indicate that IFN $\gamma$  signalling mediates pressure overload-induced BBB disruption, capillary rarefaction, and loss of pericyte's coverage. Neutralization of excessive IFN $\gamma$  activation mitigates these phenotypes, protecting mice from cerebrovascular injury.

### 3.10 Anti-IFN $\gamma$ treatment prevents cognitive impairment in pressure overload mice

Four weeks after TAC, cognitive functions of mice were assessed by the Morris Water Maze test. As expected, all experimental groups could find and reach the platform when indicated by a visual cue ([Figure 7F](#)), demonstrating that all mice had comparable visual and motor capabilities. Interestingly, during the acquisition phase of the test, while TAC mice treated with the non-relevant IgG, showed high time latencies to reach the

platform, without any improvement in their performance from day one to day three ([Figure 7G](#)), the anti-IFN $\gamma$  treatment significantly improved the performance of TAC mice, which displayed a learning curve comparable to those of Sham mice ([Figure 7G](#)). During the probe trial, TAC-anti-IFN $\gamma$  hypertensive mice displayed preserved memory, as shown by the ability of recalling where the platform was located. The same cognitive function was significantly impaired in TAC-IgG mice, which randomly swam through the quadrants ([Figure 7H and I](#)). Thus, in addition to cerebrovascular protection, blockage of IFN $\gamma$  signalling is capable of preventing pressure overload-triggered cognitive functional decline.

## 4. Discussion

The present study uncovers a mechanism by which an inflammatory signal is responsible for the development of hypertensive brain damage. Using a new zebrafish model of ion imbalance-driven RAS dysregulation, we carried out a series of gene expression analysis and live imaging to understand the time course of inflammatory disease progression and to identify cellular events involved in innate immune cell activation. We found that ion imbalance triggers RAS elevation and systemic inflammation, marked by *lfn $\gamma$*  and *il1 $\beta$*  up-regulation, leading to striking behavioural and functional alteration of macrophages/microglia and endothelial cells lining the cerebral vasculature. We observed macrophage/microglia-endothelial contact-associated endothelial junctional remodelling and retraction and lateral migration of the cells towards opposing sides of the vessel segments, leading to regression of the vessel network with no contribution of vascular cell death. Assessment of the cerebral vasculature in the TAC pressure overload mouse model further supported the occurrence of microvascular remodelling through BBB dysfunction and endothelial regression, evidenced from reduced junctional complex protein expression and lower capillary density with no change in their diameter. Endothelial regression independent of apoptosis is thought to have a role exclusively in physiological pruning of developing vascular networks.<sup>30,31,33,53</sup> Its involvement in hypertension is somewhat unexpected. The mechanisms of vascular remodelling in hypertension are largely unknown. Most studies have focused on elucidating the major changes of the arterial wall, i.e. increased lumen size and stiffness in large arteries and increased tunica media thickness with or without a reduction of lumen diameter in small arteries.<sup>54,55</sup> Adaptation and maladaptation of the vascular wall to mechanical perturbation in hypertension has been primarily linked to oxidative-stress-induced vascular smooth muscle cell activation and inflammation-driven interstitial fibrosis.<sup>54–57</sup> These earlier reported mechanisms are unlikely to be involved in the cerebral vascular regression we observed. Our findings contribute to a better mechanistic understanding of the cellular and molecular pathways underlying vascular regression during ion imbalance- and pressure overload-induced inflammatory response, which is fundamental to counteract functional deficits ensuing in the brain.

Cerebral small vessel diseases (CSVDs) are subclinical pathologies strongly associated with stroke, cognitive deterioration, and dementia.<sup>58,59</sup> Hypertension is a modifiable risk factor of CSVD.<sup>60,61</sup> The mechanisms underlying hypertension driven CSVD and the central nervous system functional decline have not been fully elucidated. Our findings, obtained from both zebrafish and mouse models, not only demonstrate a causative role of an inflammatory mediator linking the initial trigger of hypertensive response to cerebrovascular remodelling and cognitive deficit, but also unveil an underlying signalling mechanism. We showed that elevated IFN $\gamma$  expression, following RAS induction, triggers a series of pathogenic events including suppression of vasculo/neuroprotective transcriptional programme in macrophages/microglia, disruption of inter-endothelial junction, and retraction/migration-mediated cerebrovascular regression. Ultimately, the increase of neuronal cell death and the concomitant decrease of microvascular density might contribute to IFN $\gamma$ -driven cognitive deficits. The efficacy of the anti-IFN $\gamma$  treatment to prevent progression of brain vascular rarefaction and cognitive decline in the presence of hypertensive stimuli thus represents an opportunity for the development of new preventive and therapeutic strategies for hypertensive CSVD. Efficacy of anti-IFN $\gamma$  treatment in hypertension-related organ damage has been reported earlier.

In a rat model of reduced uterine perfusion pressure, administration of anti-IFN $\gamma$  has been shown to reduce placental oxidative stress and uterine artery resistive index.<sup>62</sup> IFN $\gamma$  signalling blockage, however, was not sufficient to restore diastolic dysfunction in both ion imbalance and pressure overload models, suggesting that progression from these hypertensive stimuli to cardiac remodelling might involve an IFN $\gamma$ -independent pathway. Previously, it was reported that IFN $\gamma$ -deficient mice subjected to chronic aldosterone infusion in combination with uninephrectomy and salt feeding exhibited blunted hypertension, but showed worsened diastolic dysfunction and left ventricular hypertrophy.<sup>63</sup> IFN $\gamma$  deficiency, on the other hand, reduced cardiac extracellular matrix deposition and inducible arrhythmia but did not alter blood pressure in Ang II-infused mice.<sup>64</sup> The present study, together with these earlier reports, implicates the involvement of distinctive stimuli in differential response of the heart.

In addition to IFN $\gamma$ , our work identified other potential candidates for immune modulatory, particularly macrophage-targeted, therapeutic strategy. The BMPs family of growth factors have important functions in neurogenesis, neural plasticity, and injurious response.<sup>65</sup> For example, a neuroprotective role of BMP5/7 has been reported in an  $\alpha$ -synuclein-based mouse model of Parkinson's disease.<sup>44</sup> In the vasculature, BMPs maintain homeostasis and take part in oxidative stress-triggered neangiogenesis and structural remodelling.<sup>45</sup> Ifn $\gamma$ -mediated down-regulation of bmp5 in macrophages/microglia in response to ion imbalance and prevention of cerebrovascular rarefaction by BMP5 supplementation uncovered here highlight the role of BMP5 as a critical downstream target of IFN $\gamma$ -driven innate immune derangement and brain pathology. Reduction of BMP5 expression as a result of IFN $\gamma$  induction of macrophage/microglia phenotypic alteration may underlie the disruption of endothelial junctional integrity and retraction of endothelial cells we have observed here. In line with our observations, regulation of endothelial barrier function by an anti-inflammatory population of perivascular macrophages was reported previously.<sup>66</sup> Moreover, BMP was implicated, in a partnership with yes-associated protein 1 and its paralog transcription regulator post synaptic density protein (PDZ)-binding motif (TAZ), to regulate endothelial junctional integrity through the control of VE-Cadherin turnover.<sup>67</sup> In addition to BMP, NUCB2 and its cleavage product nesfatin-1 could also exert neuroprotective function through their anti-inflammatory and anti-apoptotic properties as demonstrated in Parkinson's disease and a subarachnoid haemorrhage murine model.<sup>46,68</sup> Accordingly, a clinical study reported lower serum level of nesfatin-1 in patients with Parkinson's disease.<sup>47</sup> Involvement of nesfatin-1 in cognitive function has also been suggested.<sup>48</sup> Another molecule identified from our transcriptomic profiling is PlxnD1. Although its activation in endothelial cells can signal anti-angiogenic effect,<sup>69</sup> PlxnD1 signalling in macrophages induced vascular endothelial growth factor receptor 2-mediated pro-angiogenic response,<sup>49</sup> implicating its role in macrophage-endothelial crosstalk. Contrary to these neuro/vasculo-protective factors, a secreted enzyme found to be elevated in ion-poor-treated macrophages, carnosine dipeptidase 1 (cndp1), is directly correlated with neurodegeneration.<sup>70</sup> Our data revealing differential expression of these critical homeostatic and neuro/vasculo-protective factors, as well as neurodegenerative biomarkers in macrophages provides the first evidence linking these molecules to the innate immune cell function and pathogenesis of hypertensive brain remodelling. Moreover, alteration of these factors along with components of the complement system and antimicrobial defence mechanisms suggests that macrophages response to ion imbalance is not a prototypical pro-inflammatory activation commonly observed in acute inflammation. Derangement of macrophage homeostatic function required to maintain cell survival, stimulate vascular growth, and modulate neuronal activity under hypertensive challenge should be taken into consideration for the development of immune targeted therapies. To this end, the zebrafish model of arterial hypertension and cardiac diastolic dysfunction established here also provides new opportunities for large-scale screening of other therapeutic candidates.

## Supplementary material

Supplementary material is available at *Cardiovascular Research* online.

## Authors' contributions

Conceptualization: A.F. and S.S. Methodology: D.C., D.C.A., B.I.Z.-S., I.K.-G., L.C., M.P., M.P.K., O.A., R.C. and S.S. Funding acquisition: D.C. and S.S. Investigation: B.I. Z.-S., D.C.A., L.C., I.K.-G., M.P., M.P.K., O.A., R.C. and S.S. Project administration: D.C. and S.S. Visualization: A.F., D.C., H.-G.B., and S.S. Supervision: A.F., D.C., H.-G.B. and S.S. Writing—original draft: D.C. and S.S. Writing—review and editing: A.F., D.C., H.-G.B. and S.S.

## Acknowledgements

We thank F. Cosco, A. Banerjee, the Flow Cytometry and Advanced Light Microscopy Technology Platforms, and personnel of the Zebrafish Facility at the Max Delbrück Center for Molecular Medicine for technical support and assistance in this work. We are grateful to P.A. Morocho Jaramillo for making the graphical abstract.

**Conflict of interest:** None declared.

## Funding

This work was supported by funding from the Helmholtz-Gemeinschaft (project number VH-NG-1247), the Deutsche Forschungsgemeinschaft (DFG, German Research Foundation) – SFB-1470 – A06, and the Bundesministerium für Bildung und Forschung (project number 01KL2005) to S.S. and the Italian Ministry of Health in the framework of the European Research Area Network-Cardiovascular Diseases (ERA-CVD) Gut-brain-immune-HHD project and 'ricerca corrente' to D.C. H.-G.B. and M.P.K. are supported by grants from the Swiss National Science Foundation (310030\_200701 and 310030B\_176400) to Markus Affolter (Biozentrum, Basel).

## Data availability

Data supporting the findings of this study are available upon reasonable request to the corresponding author.

## References

- Whelton PK, Carey RM, Aronow WS, Casey DE, Collins KJ, Dennison Himmelfarb C, DePalma SM, Gidding S, Jamerson KA, Jones DW, MacLaughlin EJ, Muntner P, Ovbigele B, Smith SC, Spencer CC, Stafford RS, Taler SJ, Thomas RJ, Williams KA, Williamson JD, Wright JT, Himmelfarb CD, DePalma SM, Gidding S, Jamerson KA, Jones DW, MacLaughlin EJ, Muntner P, Ovbigele B, Smith SC, Spencer CC, Stafford RS, Taler SJ, Thomas RJ, Williams KA, Williamson JD, Wright JT, Levine GN, O'Gara PT, Halperin JL, Past I, Al SM, Beckman JA, Birtcher KK, Bozkurt B, Brindis RG, Cigarroa JE, Curtis LH, Deswal A, Fleisher LA, Gentile F, Goldberger ZD, Hlatky MA, Ikonominis J, Joglar JA, Mauri L, Pressler SJ, Riegel B, Wijeysundera DN, Walsh MN, Jacobovitz S, Oetgen WJ, Elma MA, Scholtz A, Sheehan KA, Abdullah AR, Tahir N, Warner JJ, Brown N, Robertson RM, Whitman GR, Hundley J. 2017 ACC/AHA/AAPA/ABC/ACPM/AGS/APhA/ASH/ASPC/NMA/PCNA guideline for the prevention, detection, evaluation, and management of high blood pressure in adults: a report of the American College of Cardiology/American Heart Association task force on clinical Pr. *Hypertension* 2018;**71**:e13–e115.
- Lerman LO, Kurtz TW, Touyz RM, Ellison DH, Chade AR, Crowley SD, Mattson DL, Mullins JJ, Osborn J, Eirin A, Reckelhoff JF, Iadecola C, Coffman TM. Animal models of hypertension: a scientific statement from the American heart association. *Hypertens (Dallas, Tex 1979)* 2019;**73**:e87–e120.
- Drummond GR, Vinh A, Guzik TJ, Sobey CG. Immune mechanisms of hypertension. *Nat Rev Immunol* 2019;**19**:517–532.
- Nosalski R, McGinnigle E, Siedlinski M, Guzik TJ. Novel immune mechanisms in hypertension and cardiovascular risk. *Curr Cardiovasc Risk Rep* 2017;**11**:12.
- Blacher J, Evans A, Arveiler D, Amouyel P, Ferrières J, Bingham A, Yarnell J, Haas B, Montaye M, Ruidavets J-BB, Ducimetière P. Group on behalf of the PS. Residual cardiovascular risk in treated hypertension and hyperlipidaemia: the PRIME study. *J Hum Hypertens* 2010;**24**:19–26.
- Struthers AD. A new approach to residual risk in treated hypertension-3P screening. *Hypertension* 2013;**62**:236–239.
- Caillon A, Schiffrin EL. Role of inflammation and immunity in hypertension: recent epidemiological, laboratory, and clinical evidence. *Curr Hypertens Rep* 2016;**18**:21.
- Solak Y, Afsar B, Vaziri ND, Aslan G, Yalcin CE, Covic A, Kanbay M. Hypertension as an auto-immune and inflammatory disease. *Hypertens Res* 2016;**39**:567–573.

9. Guzik TJ, Hoch NE, Brown KA, McCann LA, Rahman A, Dikalov S, Goronzy J, Weyand C, Harrison DG. Role of the T cell in the genesis of angiotensin II induced hypertension and vascular dysfunction. *J Exp Med* 2007;**204**:2449–2460.
10. Wenzel P, Knorr M, Kossmann S, Stratmann J, Hausding M, Schuhmacher S, Karbach SH, Schwenk M, Yogev N, Schulz E, Oelze M, Grabbe S, Jonuleit H, Becker C, Daiber A, Waisman A, Münzel T. Lysozyme M-positive monocytes mediate angiotensin II-induced arterial hypertension and vascular dysfunction. *Circulation* 2011;**124**:1370–1381.
11. Chan CT, Moore JP, Budzyn K, Guida E, Diep H, Vinh A, Jones ES, Widdop RE, Armitage JA, Sakkal S, Ricardo SD, Sobey CG, Drummond GR. Reversal of vascular macrophage accumulation and hypertension by a CCR2 antagonist in deoxycorticosterone/salt-treated mice. *Hypertension* 2012;**60**:1207–1212.
12. De Ciuceis C, Amiri F, Brassard P, Endemann DH, Touyz RM, Schiffrin EL. Reduced vascular remodeling, endothelial dysfunction, and oxidative stress in resistance arteries of angiotensin II-infused macrophage colony-stimulating factor-deficient mice. *Arterioscler Thromb Vasc Biol* 2005;**25**:2106–2113.
13. Leibovitz E, Ebrahimian T, Paradis P, Schiffrin EL. Aldosterone induces arterial stiffness in absence of oxidative stress and endothelial dysfunction. *J Hypertens* 2009;**27**:2192–2200.
14. Javeshghani D, Barhoumi T, Idris-Khodja N, Paradis P, Schiffrin EL. Reduced macrophage-dependent inflammation improves endothelin-1-induced vascular injury. *Hypertension* 2013;**62**:112–117.
15. Pires PW, Girgla SS, McClain JL, Kaminski NE, van Rooijen N, Dorrance AM. Improvement in middle cerebral artery structure and endothelial function in stroke-prone spontaneously hypertensive rats after macrophage depletion. *Microcirculation* 2013;**20**:650–661.
16. Faraco G, Sugiyama Y, Lane D, Garcia-Bonilla L, Chang H, Santisteban MM, Racchumi G, Murphy M, Van Rooijen N, Anrather J, Iadecola C. Perivascular macrophages mediate the neurovascular and cognitive dysfunction associated with hypertension. *J Clin Invest* 2016;**126**:4674–4689.
17. Hulsmans M, Sager HB, Roh JD, Valero-Muñoz M, Houstis NE, Iwamoto Y, Sun Y, Wilson RM, Wojtkiewicz G, Tricot B, Osborne MT, Hung J, Vinegoni C, Naxerova K, Sosnovik DE, Zile MR, Bradshaw AD, Liao R, Tawakol A, Weissleder R, Rosenzweig A, Swirski FK, Sam F, Nahrendorf M. Cardiac macrophages promote diastolic dysfunction. *J Exp Med* 2018;**215**:423–440.
18. Carnevale D, Carnevale L, Perrotta S, Pallante F, Migliaccio A, Iodice D, Perrotta M, Lembo G. Chronic 3D vascular-immune interface established by coculturing pressurized resistance arteries and immune cells. *Hypertension* 2021;**78**:1648–1661.
19. Van Linthout S, Tschöpe C. Inflammation—cause or consequence of heart failure or both? *Curr Heart Fail Rep* 2017;**14**:251–265.
20. Xiao L, Harrison DG. Inflammation in hypertension. *Can J Cardiol* 2020;**36**:635–647.
21. Aleström P, D'Angelo L, Midtlyng PJ, Schorderet DF, Schulte-Merker S, Sohm F, Warner S. Zebrafish: housing and husbandry recommendations. *Lab Anim* 2019;**51**:213–214.
22. Kumai Y, Bernier NJ, Perry SF. Angiotensin-II promotes na<sup>+</sup> uptake in larval zebrafish, *Danio rerio*, in acidic and ion-poor water. *J Endocrinol* 2014;**220**:195–205.
23. Ahmetoğlu A, Erdöl H, Şimşek A, Gökçe M, Dinç H, Gümele HR, Ahmetoğlu A, Erdöl H, Şimşek A, Gökçe M, Dinç H, Gümele HR. Effect of hypertension and candesartan on the blood flow velocity of the extraocular vessels in hypertensive patients. *Eur J Ultrasound* 2003;**16**:177–182.
24. Wolf S, Arend O, Schulte K, Ittel TH, Reim M. Quantification of retinal capillary density and flow velocity in patients with essential hypertension. *Hypertension* 1994;**23**:464–467.
25. Chuang S-YY, Cheng H-MM, Mitchell GF, Sung S-HH, Chen C-HH, Pan W-HH, Hwang A-CC, Chen L-KK, Wang P-NN. Carotid flow velocities and blood pressures are independently associated with cognitive function. *Am J Hypertens* 2019;**32**:289–297.
26. Tsubata H, Nakanishi N, Itatani K, Ogo T, Yaku H, Matoba S. Pulmonary artery blood flow dynamics in patients with chronic thromboembolic pulmonary hypertension; analysis by computational fluid dynamics. *Eur Respir J* 2019;**54**:PA1435.
27. Yang T, Xu C. Physiology and pathophysiology of the intrarenal renin-angiotensin system: an update. *J Am Soc Nephrol* 2017;**28**:1040–1049.
28. Schiattarella GG, Hill JA. Is inhibition of hypertrophy a good therapeutic strategy in ventricular pressure overload? *Circulation* 2015;**131**:1435–1447.
29. Heinzl FR, Hohendanner F, Jin G, Sedej S, Edelmann F. Myocardial hypertrophy and its role in heart failure with preserved ejection fraction. *J Appl Physiol* 2015;**119**:1233–1242.
30. Chen Q, Jiang L, Li C, Hu D, Bu J, Cai D, Du J. Haemodynamics-driven developmental pruning of brain vasculature in zebrafish. *PLoS Biol* 2012;**10**:e1001374.
31. Franco CA, Jones ML, Bernabeu MO, Geudens I, Mathivet T, Rosa A, Lopes FM, Lima AP, Ragab A, Collins RT, Phng L-KK, Coveney PV, Gerhardt H. Correction: dynamic endothelial cell rearrangements drive developmental vessel regression (PLoS Biol, 2015). *PLoS Biol* 2015;**13**:e1002125.
32. Santisteban MM, Ahn SJ, Lane D, Faraco G, Garcia-Bonilla L, Racchumi G, Poon C, Schaeffer S, Segarra SG, Körbelin J, Anrather J, Iadecola C. Endothelium-macrophage crosstalk mediates blood-brain barrier dysfunction in hypertension. *Hypertension* 2020;**76**:795–807.
33. Lenard A, Daetwyler S, Betz C, Ellertsdottir E, Belting H-GG, Huisken J, Affolter M. Endothelial cell self-fusion during vascular pruning. *PLoS Biol* 2015;**13**:e1002126.
34. Sava RI, Pepine CJ, March KL. Immune dysregulation in HFpEF: a target for mesenchymal stem/stromal cell therapy. *J Clin Med* 2020;**9**:241.
35. Ye J, Que B, Huang Y, Lin Y, Chen J, Liu L, Shi Y, Wang Y, Wang M, Zeng T, Wang Z, Hu H, Xu Y, Shi L, Ye D, Liu J, Jiang H, Wan J, Ji Q. Interleukin-12p35 knockout promotes macrophage differentiation, aggravates vascular dysfunction, and elevates blood pressure in angiotensin II-infused mice. *Cardiovasc Res* 2019;**115**:1102–1113.
36. Sesso HD, Jiménez MC, Wang L, Ridker PM, Buring JE, Gaziano JM. Plasma inflammatory markers and the risk of developing hypertension in men. *J Am Heart Assoc* 2015;**4**:e001802.
37. Mosser DM, Edwards JP. Exploring the full spectrum of macrophage activation. *Nat Rev Immunol* 2008;**8**:958–969.
38. Pelegrin P, Surprenant A. Dynamics of macrophage polarization reveal new mechanism to inhibit IL-1 $\beta$  release through pyrophosphates. *EMBO J* 2009;**28**:2114–2127.
39. Ferreira VP, Pangburn MK, Cortés C. Complement control protein factor H: the good, the bad, and the inadequate. *Mol Immunol* 2010;**47**:2187–2197.
40. Chen J, Huddleston J, Buckley RM, Malig M, Lawhon SD, Skow LC, Lee MO, Eichler EE, Andersson L, Womack JE. Bovine NK-lysin: copy number variation and functional diversification. *Proc Natl Acad Sci U S A* 2015;**112**:E7223–E7229.
41. Okamori S, Ishii M, Asakura T, Suzuki S, Namkoong H, Kagawa S, Hegab AE, Yagi K, Kamata H, Kusumoto T, Ogawa T, Takahashi H, Yoda M, Horiuchi K, Hasegawa N, Fukunaga K. ADAM10 Partially protects mice against influenza pneumonia by suppressing specific myeloid cell population. *Am J Physiol Cell Mol Physiol* 2021;**321**:L872–L884.
42. Andou A, Hisamatsu T, Okamoto S, Chinen H, Kamada N, Kobayashi T, Hashimoto M, Okutsu T, Shimbo K, Takeda T, Matsumoto H, Sato A, Ohtsu H, Suzuki M, Hibi T. Dietary histidine ameliorates murine colitis by inhibition of proinflammatory cytokine production from macrophages. *Gastroenterology* 2009;**136**:564–74.e2.
43. Zheng L, Xu H, Di Y, Chen L, Liu J, Kang L, Gao L. ELK4 promotes the development of gastric cancer by inducing M2 polarization of macrophages through regulation of the KDM5A-PJA2-KSR1 axis. *J Transl Med* 2021;**19**:342.
44. Vitic Z, Safory H, Jovanovic VM, Sarusi Y, Stavsky A, Kahn J, Kuzmina A, Tokar L, Gitler D, Taube R, Friedel RH, Engelender S, Brodski C. BMP5/7 protect dopaminergic neurons in an  $\alpha$ -synuclein mouse model of Parkinson's disease. *Brain* 2021;**144**:e15–e15.
45. Goumans MJ, Zwijsen A, ten Dijke P, Bailly S. Bone morphogenetic proteins in vascular homeostasis and disease. *Cold Spring Harb Perspect Biol* 2018;**10**:a031989.
46. Shen XL, Song N, Du XX, Li Y, Xie JX, Jiang H. Nesfatin-1 protects dopaminergic neurons against MPP<sup>+</sup>/MPTP-induced neurotoxicity through the C-raf-ERK1/2-dependent anti-apoptotic pathway. *Sci Rep* 2017;**7**:40961.
47. Emir GK, Ünal Y, Yılmaz N, Tosun K, Kutlu G. The association of low levels of nesfatin-1 and glucagon-like peptide-1 with oxidative stress in Parkinson's disease. *Neurol Sci* 2019;**40**:2529–2535.
48. Pałasz A, Krzystanek M, Worthington J, Czajkowska B, Kostro K, Wierkiewicz R, Bajor G. Nesfatin-1, a unique regulatory neuropeptide of the brain. *Neuropeptides* 2012;**46**:105–112.
49. Meda C, Molla F, De Pizzol M, Regano D, Maione F, Capano S, Locati M, Mantovani A, Latini R, Bussoletto F, Giraudo E. Semaphorin 4A exerts a proangiogenic effect by enhancing vascular endothelial growth factor- $\alpha$  expression in macrophages. *J Immunol* 2012;**188**:4081–4092.
50. Sawamiphak S, Kontarakis Z, Stainer DYR. Interferon gamma signaling positively regulates hematopoietic stem cell emergence. *Dev Cell* 2014;**31**:640–653.
51. Carnevale D, Mascio G, Ajmone-Cat MA, D'Andrea I, Cifelli G, Madonna M, Cocozza G, Frati A, Carullo P, Carnevale L, Alleva E, Branchi I, Lembo G, Minghetti L. Role of neuroinflammation in hypertension-induced brain amyloid pathology. *Neurobiol Aging* 2012;**33**:e19–e29.
52. Carnevale D, Mascio G, D'Andrea I, Fardella V, Bell RD, Branchi I, Pallante F, Zlokovic B, Yan SS, Lembo G. Hypertension induces brain  $\beta$ -amyloid accumulation, cognitive impairment, and memory deterioration through activation of receptor for advanced glycation end products in brain vasculature. *Hypertension* 2012;**60**:188–197.
53. Kochhan E, Lenard A, Ellertsdottir E, Herwig L, Affolter M, Belting H-G, Siekmann AF. Blood flow changes coincide with cellular rearrangements during blood vessel pruning in zebrafish embryos. *PLoS One* 2013;**8**:e75060.
54. Schiffrin EL. Vascular remodeling in hypertension: mechanisms and treatment. *Hypertension* 2012;**59**:367–374.
55. Humphrey JD. Mechanisms of vascular remodeling in hypertension. *Am J Hypertens* 2021;**34**:432–441.
56. Marchesi C, Rehman A, Rautureau Y, Kasal DA, Briet M, Leibowitz A, Simeoni SMC, Ebrahimian T, Neves MF, Offermanns S, Gonzalez FJ, Paradis P, Schiffrin EL. Protective role of vascular smooth muscle cell PPAR $\gamma$  in angiotensin II-induced vascular disease. *Cardiovasc Res* 2013;**97**:562–570.
57. Wu J, Thabet SR, Kirabo A, Trott DW, Saleh MA, Xiao L, Madhur MS, Chen W, Harrison DG. Inflammation and mechanical stretch promote aortic stiffening in hypertension through activation of p38 mitogen-activated protein kinase. *Circ Res* 2014;**114**:616–625.
58. Wardlaw JM, Smith EE, Biessels GJ, Cordonnier C, Fazekas F, Frayne R, Lindley RI, O'Brien JT, Barkhof F, Benavente OR, Black SE, Brayne C, Breteler M, Chabriat H, Decarli C, de Leeuw F-E, Doubal F, Duering M, Fox NC, Greenberg S, Hachinski V, Kilimann I, Mok V, van Oostenbrugge R, Pantoni L, Speck O, Stephan BCM, Teipel S, Viswanathan A, Werring D, Chen C, Smith C, van Buchem M, Norrving B, Gorelick PB, Dichgans M. Neuroimaging standards for research into small vessel disease and its contribution to ageing and neurodegeneration. *Lancet Neurol* 2013;**12**:822–838.
59. Pavlovic AM, Pekmezovic T, Trajkovic JZ, Tomic G, Cvitan E, Sternic N. Increased risk of cognitive impairment and more severe brain lesions in hypertensive compared to non-hypertensive patients with cerebral small vessel disease. *J Clin Hypertens (Greenwich)* 2018;**20**:1260–1265.
60. Nam K-WW, Kwon HH-MM, Jeong H-YY, Park J-HH, Kwon HH-MM, Jeong S-MM. Cerebral small vessel disease and stage 1 hypertension defined by the 2017 American College of Cardiology/American Heart Association guidelines. *Hypertension* 2019;**73**:1210–1216.

61. Ma Y, Song A, Viswanathan A, Blacker D, Vernooij MW, Hofman A, Papatheodorou S. Blood pressure variability and cerebral small vessel disease: a systematic review and meta-analysis of population-based cohorts. *Stroke* 2020;**51**:82–89.
62. Travis OK, Tardo GA, Giachelli C, Siddiq S, Nguyen HT, Crosby MT, Johnson TD, Brown AK, Booz GW, Smith AN, Williams JM, Cornelius DC. Interferon  $\gamma$  neutralization reduces blood pressure, uterine artery resistance index, and placental oxidative stress in placental ischemic rats. *Am J Physiol Integr Comp Physiol* 2021;**321**:R112–R124.
63. Garcia AG, Wilson RM, Heo J, Murthy NR, Baid S, Ouchi N, Sam F. Interferon- $\gamma$  ablation exacerbates myocardial hypertrophy in diastolic heart failure. *Am J Physiol Hear Circ Physiol* 2012;**303**:H587–H596.
64. Markó L, Kvakán H, Park J-KK, Qadri F, Spallek B, Binger KJ, Bowman EP, Kleinewietfeld M, Fokuhl V, Dechend R, Müller DN. Interferon- $\gamma$  signaling inhibition ameliorates angiotensin ii-induced cardiac damage. *Hypertension* 2012;**60**:1430–1436.
65. Jensen GS, Leon-Palmer NE, Townsend KL. Bone morphogenetic proteins (BMPs) in the central regulation of energy balance and adult neural plasticity. *Metabolism* 2021;**123**:154837.
66. He H, Mack JJ, Güç E, Warren CM, Squadrito ML, Kilarski VV, Baer C, Freshman RD, McDonald AI, Ziyad S, Swartz MA, De Palma M, Iruela-Arispe ML. Perivascular macrophages limit permeability. *Arterioscler Thromb Vasc Biol* 2016;**36**:2203–2212.
67. Neto F, Klaus-Bergmann A, Ong YT, Alt S, Vion A-C, Szymborska A, Carvalho JR, Hollfänger I, Bartels-Klein E, Franco CA, Potente M, Gerhardt H. YAP And TAZ regulate adherens junction dynamics and endothelial cell distribution during vascular development. *Elife* 2018;**7**:e31037.
68. Özsavcı D, Erşahin M, Şener A, Özakpınar ÖB, Toklu HZ, Akakin D, Şener G, Yeğen BÇ. The novel function of nesfatin-1 as an anti-inflammatory and antiapoptotic peptide in sub-arachnoid hemorrhage-induced oxidative brain damage in rats. *Neurosurgery* 2011;**68**:1699–1708.
69. Yang W, Hu J, Uemura A, Tetzlaff F, Augustin HG, Fischer A. Semaphorin-3C signals through neuropilin-1 and PlexinD1 receptors to inhibit pathological angiogenesis. *EMBO Mol Med* 2015;**7**:1267–1284.
70. Heywood WE, Galimberti D, Bliss E, Sirka E, Paterson RW, Magdalinou NK, Carecchio M, Reid E, Heslegrave A, Fenoglio C, Scarpini E, Schott JM, Fox NC, Hardy J, Bahtia K, Heales S, Sebire NJ, Zetterburg H, Mills K. Identification of novel CSF biomarkers for neurodegeneration and their validation by a high-throughput multiplexed targeted proteomic assay. *Mol Neurodegener* 2015;**10**:64.

## Translational perspective

Hypertension is a major risk factor for damages of the vasculature, heart, and brain and thereby a major healthcare burden. Inadequate cerebral blood supply due to altered cerebrovascular structure and vasoregulatory disruption upon hypertension render the brain highly susceptible to stroke and cognitive decline. We envision that the cellular and molecular mechanisms uncovered here linking immune dysregulation to cerebrovascular remodeling and functional impairment of the brain will inform future development of immunomodulatory therapeutic strategies for counteracting derangement of macrophage/microglia activation and their vasculo/neuroprotective function in response to systemic inflammation in hypertension.